UCLouvain

epl

École polytechnique de Louvain

Three-dimensional segmentation and structural characterization of murine atherosclerotic plaques using contrast-enhanced microCT

Author: **Madeleine de Rosen de Borgharen**
Supervisors: **Mandy Grootaert, Greet Kerckhofs**
Readers: **Alice Marino, Pierre Schneidewind**
Academic year 2025–2026
Master [120] in Biomedical Engineering

This thesis utilized OpenAI's ChatGPT for assistance in sentence redaction and improvement.

Acknowledgments

First and foremost, I would like to express my gratitude to my supervisors, Professor Greet Kerckhofs and Professor Mandy Grootaert, for their invaluable guidance, trust, and support throughout this master's thesis. I am grateful for their constant availability, their feedback, and the time they dedicated to guiding my research, which allowed me to complete this project in the best possible conditions.

I would also like to extend my thanks to Pierre Schneidewind for his essential technical support. Thank you for your help with the scans, your availability and for always taking the time to answer my questions. My gratitude also goes to the entire Contrast Team for welcoming me and providing a collaborative and stimulating environment.

Finally, I am deeply grateful to my family and friends for their unconditional support. I want to thank my parents, my brother, and my sister for always believing in me, not only during this thesis project but throughout my entire academic journey. Your constant encouragement has been my greatest strength. To my friends, thank you for your unwavering support, your valuable advice, and for all the great time spent together.

Abstract

Atherosclerosis is a chronic inflammatory disease and the leading cause of cardiovascular mortality worldwide. Accurate three-dimensional characterization of atherosclerotic plaques remains a challenge, as conventional 2D histology suffers from tissue destruction and sampling bias. This thesis evaluates the potential of contrast-enhanced micro-computed tomography (CECT) to visualize and quantify plaque architecture within the intact murine aortic root.

Atherosclerosis was induced in female mice using the AAV8-mPCSK9 model combined with a high-fat diet over 10 weeks. Ex vivo CECT imaging was performed at a voxel size of 1.35 µm using Hf-WD POM 1:2 as a contrast-enhancing staining agent. A dedicated preprocessing and segmentation pipeline was developed in Avizo, combining intensity normalization, median and unsharp masking filters, marker-controlled watershed segmentation, and manual intensity thresholding to classify distinct tissue compartments.

The resulting gray-level distributions were validated through qualitative correlation with Sirius Red histological sections obtained from biologically equivalent animals. The intensity classes identified in CECT were mapped to specific tissue components, including the lipid-rich necrotic core, the developing fibrous cap, the healthy vascular wall, and the dense elastic laminae of the tunica media. In the early stage group, a consistent volumetric expansion of the aortic wall was observed relative to healthy controls, accompanied by the emergence of lower attenuation density profiles associated with pathological remodeling. Quantitative morphometric indices, including plaque burden, necrotic core volume fraction, and core-to-cap ratio, revealed marked phenotypic heterogeneity within the cohort. Marked phenotypic heterogeneity was observed within the cohort, with lesion profiles ranging from lipid-dominant to transitional fibro-calcific configurations. These findings demonstrate that high-resolution CECT is a promising tool for the 3D morphometric profiling of atherosclerotic plaques in preclinical research.

Contents

List of Figures xii

List of Tables xiii

List of Abbreviations xiii

Introduction 1

I State of the art 3

1 Atherosclerosis 5
1.1 Pathophysiology of plaque formation 5
1.2 Plaque regression, stabilization and rupture 7
1.2.1 Stable versus vulnerable atherosclerotic plaques 8
1.2.2 Mechanisms of plaque destabilization and rupture 10
1.3 Current therapeutic strategies 11

2 Experimental mouse models for atherosclerosis 13
2.1 The Apolipoprotein E deficient model 14
2.2 The Low-density lipoprotein receptor-deficient model 15
2.3 ApoE3-Leiden transgenic model 15
2.4 Adeno-associated virus stereotype 8 mediated PCSK9 expression model 16

3 Imaging techniques for plaque characterization in mice models 19
3.1 In vivo imaging techniques 19
3.1.1 Ultrasound biomicroscopy 19
3.1.2 Magnetic resonance imaging 20
3.1.3 Positron emission tomography/Single photon emission computed tomography 21

3.1.4 Photoacoustic imaging 22
3.2 Ex vivo imaging techniques 24
3.2.1 Classical two-dimensional histology 24
3.2.1.1 General principles of histological analysis 24
3.2.1.2 Classical two dimension histology for the characterization of atherosclerosis in mouse models 25
3.2.1.3 Limitations of classical two dimension histology for plaque analysis 26
3.2.2 X-ray Microfocus-computed tomography and contrast-enhanced microCT for plaque characterization 27
3.2.2.1 X-ray microfocus-computed tomography 27
3.2.2.2 Contrast-enhanced microCT 29

4 Problem statement, general aim and objectives 33

II Methodology 35

5 Materials and methods 37
5.1 Study design 37
5.2 Sample preparation 37
5.3 CECT image acquisition and reconstruction 38
5.4 Image preprocessing 39
5.5 Image segmentation workflow 40

III Results and discussion 45

6 Results 47
6.1 3D visualization of the aortic root 47
6.2 Intensity-based tissue classification 49
6.3 Histological correlation 51
6.4 Volumetric analysis of plaque components 54

7 Discussion 57
7.1 Physico-chemical basis of CECT and histological validation 57
7.2 Plaque characterization and volumetric interpretation of lesion vulnerability 58
7.3 Analysis of tissue mineralization and calcification mapping 60

8 Conclusion and future perspectives 63
8.1 General conclusion 63

8.2 Methodological and biological limitations 64
8.3 Future perspectives 65

A Additional segmentation results **67**

B Additional 3D visualisation results **69**

Bibliography **78**

List of Figures

1.1 Schematic overview of atherosclerotic plaque development. See text for explanation. Green arrows indicate stimulation of the indicated process [5]. 6
1.2 Representative examples of stable atherosclerotic plaques observed in histology, including A: healed plaque rupture, B: chronic total occlusions and C: fibro-calcified plaques. These images illustrate lesions characterized by a more structured tissue organization and increased stability compared to vulnerable plaques. Standard histological stains (Movat pentachrome and haematoxylin-eosin)[7]. 9
1.3 Representative examples of unstable atherosclerotic human plaques observed in histology, including A: thin-cap fibroatheroma, B: intraplaque hemorhage, C: plaque fissure, D: plaque rupture, E: plaque erosion, and F: calcified nodules. The images illustrate the diversity of plaque destabilization mechanisms associated with acute coronary syndrome [7]. 10

3.1 Photoacoustic imaging of mouse atherosclerotic lesions. Representative images of the unmixed photoacoustic signal of Evans Blue, macrophages, lipids, and collagen, respectively, in 3D in vivo scans of a mouse bearing advanced lesions (panels A-D). Representative images of the unmixed photoacoustic signal of the above-mentioned molecules or dyes, in 3D ex vivo scans of mice displayed in (A–D) (panels E-H). (Adapted from [27]). 23

3.2 Histological classification of atherosclerotic lesion severity in the mouse aortic root. Representative images of sections stained with hematoxylin–phloxine–saffron. Lesions are categorized into mild (Types I–III) and severe (Types IV–V) plaques. Yellow outlines delineate the circumference of each lesion. Abbreviations indicate: FO = foam cells extending into the media; CA = fibrotic cap; I = infiltration into the media; FI = fibrosis; L = breach in the elastic lamina; CR = cholesterol crystals. Scale bars = 200 µm. (Adapted from [5]). 26
3.3 Representative paired histological (left) and microCT (right) sections illustrating the agreement between imaging modalities. p: plaque; L: lumen; w: wall; scale bar = 400 µm. (Adapted from [44]). 30

5.1 Pre-processing filtering steps illustrated using a representative cross-section (slice 777) of sample LS58. Scale bars: 500 µm. Anatomical orientation: A: anterior, P: posterior, L: left, R: right. 40
5.2 Image segmentation workflow illustrated with a representative cross-section (slice 777) of the sample LS58. Scale bars: 100 µm (500 µm for (a)) Anatomical orientation: A: anterior, P: posterior, L: left, R: right. 42
5.3 Grayscale intensity histograms of the CECT imaging of the early stage sample LS58 used to define thresholding values for multi-class segmentation. Left: Complete histogram plotted on a logarithmic scale. Right: Histogram plotted on a linear scale (excluding the peak at 0) to isolate the overlapping peaks. The vertical dashed lines indicate the selected multi-thresholding intensity values (75, 95, 105, 130, and 180). 43
5.4 Grayscale intensity histograms of the CECT imaging of the control sample LS90 used to define thresholding values for multi-class segmentation. Left: Complete histogram plotted on a logarithmic scale. Right: Histogram plotted on a linear scale (excluding the peak at 0) to isolate the overlapping peaks. The vertical dashed lines indicate the selected multi-thresholding intensity values (75, 95, 105, 130, and 180). 44

6.1 3D visualization of a control sample (LS90). (a) Raw 3D CECT sagittal view. (b) Segmented 3D sagittal view showing density distribution. (c, d) QR codes to access the respective reconstructed videos. Scale bar: 200 µm. Anatomical orientation: S: Superior, I: Inferior, A: Anterior, P: Posterior. 48

6.2 3D visualization of an early stage sample (LS58). (a) Raw 3D CECT sagittal view. (b) Segmented 3D sagittal view showing density distribution. (c, d) QR codes to access the respective reconstructed videos. Scale bar: 200 µm. Anatomical orientation: S: Superior, I: Inferior, A: Anterior, P: Posterior. 49
6.3 Cumulative bar chart highlighting the total volume and internal segmentation of the aortic wall for early stage (LS58, LS59, LS60) and control (LS90, LS93) samples. 50
6.4 Qualitative correlation between CECT cross-sections and reference 2D Sirius Red histological views. (a) Segmented CECT axial slice of a control sample (LS90, slice 1360) and (b) a control Sirius Red histological section. (c) Segmented CECT axial slice of an early stage sample (LS58, slice 1000) and (d) an early stage histological section. Scale bars: 100 µm (a, c), 200 µm (b, d). Orientation: A: anterior, P: posterior, L: left, R: right. 52
6.5 CECT identification of calcified regions. (a) 2D structural view. (b) Segmented cross-section highlighting the calcifications (orange) embedded within the plaque tissue. (c) `https://youtu.be/kFWDeSqCTqs`. Scale bars: 200 µm. Orientation: A: anterior, P: posterior, L: left, R: right. 54
6.6 Relative volumetric composition of murine aortic root plaques. Stacked bar plot representing the percentage distribution of tissue components (Elastic laminae, Leaflet, Fibrous cap, Necrotic core, Calcification) for samples LS58, LS59, and LS60. 55

A.1 Grayscale intensity histograms of the CECT imaging of the early stage sample LS59 used to define thresholding values for multi-class segmentation. (Left) Complete histogram plotted on a logarithmic scale. (Right) Histogram plotted on a linear scale (excluding the peak at 0) to isolate the overlapping peaks. The vertical dashed lines indicate the selected multi-thresholding intensity values (75, 95, 105, 130, and 180). 67
A.2 Grayscale intensity histograms of the CECT imaging of the early stage sampe LS60 used to define thresholding values for multi-class segmentation. (Left) Complete histogram plotted on a logarithmic scale. (Right) Histogram plotted on a linear scale (excluding the peak at 0) to isolate the overlapping peaks. The vertical dashed lines indicate the selected multi-thresholding intensity values (75, 95, 105, 130, and 180). 68

B.1 QR code linking to the complete 3D visualization and video playlist of the analyzed aortic roots. https://www.youtube.com/playlist?list=PLuRBcrA7AEgqrs15Br4lzea03sx2KtEGo 69
B.2 3D visualization of a control sample (LS93). (a) Raw 3D CECT coronal view. (b) Segmented 3D coronal view showing density distribution. (c, d) QR codes to access the respective reconstructed videos. Scale bar: 200 µm. Anatomical orientation: S: Superior, I: Inferior, R: Right, L: Left. 70
B.3 3D visualization of an early stage sample (LS59). (a) Raw 3D CECT coronal view. (b) Segmented 3D coronal view showing density distribution. (c, d) QR codes to access the respective reconstructed videos. Scale bar: 200 µm. Anatomical orientation: S: Superior, I: Inferior, R: Right, L: Left. 71
B.4 3D visualization of an early stage sample (LS60). (a) Raw 3D CECT coronal view. (b) Segmented 3D coronal view showing density distribution. (c, d) QR codes to access the respective reconstructed videos. Scale bar: 200 µm. Anatomical orientation: S: Superior, I: Inferior, R: Right, L: Left. 72

List of Tables

5.1 Summary of CECT acquisition and reconstruction parameters used for all samples. 39
5.2 Intensity ranges used for manual threshold-based segmentation. . . 43

6.1 Volumetric measurements (mm^3) of the defined gray value classes within the aortic wall for early stage (LS58, LS59, LS60) and control (LS90, LS93) samples. 50
6.2 Quantitative volumetric analysis (mm^3) of vascular wall and plaque components within the early stage group. 55
6.3 Plaque vulnerability and burden indices across the early stage group. Plaque burden: plaque volume/total vessel volume (%). Necrotic core volume fraction: Necrotic core volume/total plaque volume (%). Core-to-cap ratio: volume ratio between the necrotic core and the fibrous cap. 56

List of Abbreviations

18F-FDG fluorine-18 fluorodeoxyglucose.

18F-NaF fluorine-18 sodium fluoride.

2D two dimensions.

3D three dimensions.

AAV8-mPCSK9 adeno-associated virus stereotype 8 mediated PCSK9 expression.

ACS acute coronary syndromes.

ApoB apolipoprotein B.

ApoE apolipoprotein E.

ApoE$^{-/-}$ apolipoprotein E deficient model.

CECT contrast-enhanced X-ray microfocus-computed tomography.

CESA contrast-enhancing staining agent.

CETP cholesteryl ester transfer protein.

CN calcified nodules.

CT computed tomography.

CTO chronic total occlusions.

ECM extracellular matrix.

HDL high-density lipoprotein.

Hf-WD POM 1:2 hafnium-substituted Wells-Dawson 1:2 polyoxometalate.

HPR healed plaque ruptures.

ICAM-1 intercellular adhesion molecule-1.

LDL low-density lipoprotein.

LDLR low-density lipoprotein receptor.

LDLr$^{-/-}$ low-density lipoprotein receptor-deficient model.

microCT X-ray microfocus-computed tomography.

MRI magnetic resonance imaging.

oxLDL oxidized low-density lipoprotein.

PAI photoacoustic imaging.

PAV percentage atheroma volume.

PBS phosphate-buffered saline.

PCSK9 proprotein convertase subtilisin/kexin type 9.

PET positron emission tomography.

POM polyoxometalate.

PTA phosphotungstic acid.

ROI region of interest.

SMC smooth muscle cell.

SPECT single photon emission computed tomography.

TAV total atheroma volume.

TCFA thin-cap fibroatheromas.

UBM ultrasound biomicroscopy.

VCAM-1 vascular cell adhesion molecule-1.

VLDL very-low-density lipoprotein.

Introduction

Atherosclerosis is the leading cause of cardiovascular morbidity and mortality worldwide and underlies most major cardiovascular events, including myocardial infarction and ischemic stroke. The disease is characterized by the progressive accumulation of lipids, inflammatory cells, fibrotic tissue, and calcifications within the arterial wall, leading to the formation of complex atherosclerotic plaques. Beyond simple arterial narrowing, the composition and structural organization of these lesions play a critical role in determining plaque stability and clinical risk.

Understanding the development and structural heterogeneity of atherosclerotic plaques is therefore a major objective in cardiovascular research. In this context, experimental mouse models have become essential tools for studying the mechanisms involved in plaque progression and for evaluating emerging therapeutic strategies. However, accurately characterizing these lesions remains technically challenging due to the complex three dimensions (3D) organization, and heterogeneous composition.

Recent advances in imaging technologies have opened new possibilities for the non-destructive visualization of vascular tissues. In particular, contrast-enhanced X-ray microfocus-computed tomography (CECT) enables high-resolution 3D imaging of intact biological samples while improving soft tissue contrast. This technique therefore represents a promising approach for the volumetric characterization of atherosclerotic plaques and vascular remodeling.

The aim of this thesis is to explore the potential of CECT for the 3D structural characterization of murine atherosclerotic plaques in the aortic root. To achieve this, a dedicated image preprocessing and segmentation workflow was developed in order to investigate tissue organization, plaque composition, and volumetric heterogeneity within the vascular wall.

Part I

State of the art

Chapter 1

Atherosclerosis

Atherosclerosis is a chronic inflammatory disease that begins early in life and is characterized by the accumulation of lipids within the artery walls. Over time, this accumulation leads to the formation of atherosclerotic plaques, which cause a gradual narrowing of the arterial lumen. These plaques may remain stable for many years but can suddenly become unstable, rupture, and lead to thrombus formation [1]. It is the leading cause of cardiovascular morbidity and mortality worldwide and is directly associated with an increased risk of major cardiovascular events [2]. This risk is exacerbated by several key factors, including hyperlipidemia, an unhealthy diet, smoking, and physical inactivity [3, 4]. The most severe complications include myocardial infarction, resulting from plaque rupture in the coronary arteries, and ischemic stroke, caused by atherosclerotic damage of the carotid or cerebral arteries and subsequent thrombus embolization [1]. Therefore, the assessment and management of atherosclerotic plaques are essential not only for the prevention, but also for the diagnosis and treatment of cardiovascular disease, with plaque stabilization and regression representing key therapeutic goals.

1.1 Pathophysiology of plaque formation

The formation of atherosclerotic plaques (Figure 1.1) results from a complex interaction between lipid deposition, inflammatory changes, cell migration and proliferation, and arterial wall damage [2]. Atherosclerosis is based on two complementary mechanisms: the accumulation of lipoproteins in the arterial intima and the activation of the inflammatory process, characterized by the infiltration of circulating monocytes into the plaques that are forming. This inflammatory recruitment is driven by endothelial dysfunction, which increases the permeability of the arterial wall and the expression of adhesion molecules. These two components

are closely linked and contribute together to the development and progression of the disease [5].

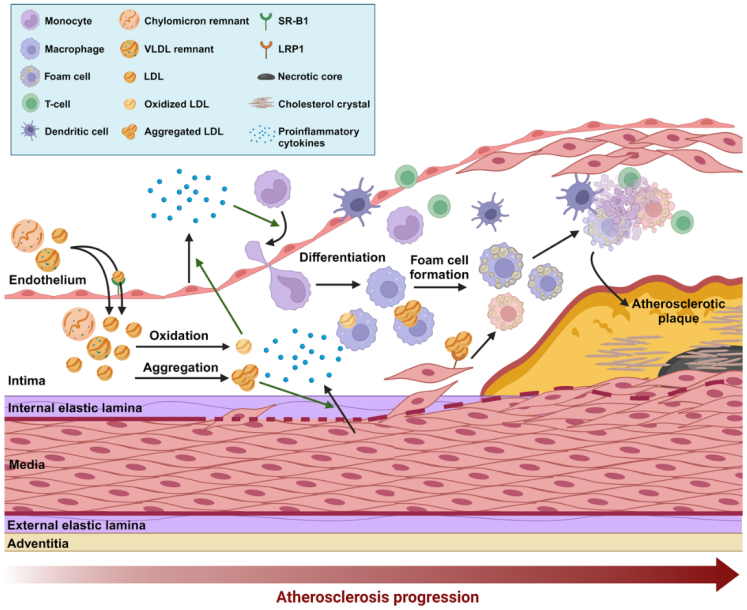


Figure 1.1: Schematic overview of atherosclerotic plaque development. See text for explanation. Green arrows indicate stimulation of the indicated process [5].

Lipoproteins are particles that transport lipids (triglycerides and cholesterol) in the blood. They mainly include chylomicrons, very-low-density lipoprotein (VLDL), low-density lipoprotein (LDL), and high-density lipoprotein (HDL). Under normal conditions, these lipoproteins circulate in the blood and supply lipids to tissues for energy or cell membrane construction [5]. In certain metabolic disorders, the liver may produce excess VLDL, and/or the metabolism and elimination of lipoproteins containing apolipoprotein B (ApoB) (chylomicrons, VLDL, and LDL) may be disrupted. This leads to an accumulation of triglycerides and cholesterol esters carried by these lipoproteins in the blood, a phenomenon known as combined hyperlipidemia [5].

Lipoproteins containing ApoB are proatherogenic, because they can cross the arterial endothelium through paracellular transport (“paracytosis”) and penetrate the arterial intima [5]. This marks the beginning of plaque formation, as LDL particles start to accumulate in this inner layer. Once in the intima, LDL can undergo enzymatic or non-enzymatic oxidation [1, 5, 6].

In response to this accumulation and oxidation, endothelial cells and smooth muscle cells (SMCs) become activated, triggering a local inflammatory process. This activation results in increased expression of adhesion molecules (such as intercellular adhesion molecule-1 (ICAM-1) and vascular cell adhesion molecule-1 (VCAM-1)) that allow immune cells to attach to the endothelium and the production of chemokines that attract immune cells to the intima [5]. These signals promote the infiltration of circulating monocytes and T lymphocytes directly into the arterial wall [1, 5].

Once recruited into the inflamed wall, monocytes differentiate into macrophages. Stimulated by pro-inflammatory cytokines, these macrophages attempt to eliminate trapped lipids, particularly oxidized low-density lipoprotein (oxLDL). When the amount of lipids in these cells increases excessively, they become foam cells. These cells represent the first visible structure of atherosclerotic plaque, called a lipid streak [1, 5]. Foam cells play a key role in atherosclerotic plaque development by releasing inflammatory mediators that promote plaque growth. Macrophages also participate in the regulation of inflammation and tissue repair [7]. In early lesions, the accumulation of foam cells, lipids, and cellular debris forms the basis of the atheroma [1]. At the same time, the inflammatory response stimulates SMCs in the tunica media to migrate to the subendothelial space. As shown in Figure 1.1, these SMCs can also take up lipids and differentiate into foam cells, contributing further to the plaque's cellular composition. These cells proliferate and produce extracellular matrix (ECM) proteins, strengthening and thickening the plaque [1].

As plaque progresses, the process of efferocytosis (the removal of dead or dying cells) becomes ineffective. Unremoved foam cells and lipid debris accumulate in the center of the plaque, forming a lipid-rich necrotic core [2]. This core is a major feature of mature atheroma and contributes to the vulnerability of the plaque, increasing the risk of rupture and cardiovascular events. At the same time, a fibrous layer consisting of collagen, proteoglycans, and SMCs develops on the surface of the lesion. This fibrous cap is essential for maintaining the stability of the plaque. However, foam cells secrete enzymes capable of degrading the ECM. This degradation gradually weakens the fibrous cap, making the plaque more vulnerable and increasing the risk of rupture [5].

1.2 Plaque regression, stabilization and rupture

Not all atherosclerotic plaques pose the same risk of clinical complications. Their structure, composition, and inflammatory activity largely determine their stability. There are two different types of plaques: stable plaques and unstable plaques [7].

1.2.1 Stable versus vulnerable atherosclerotic plaques

Stable plaques represent the most consolidated and healed forms of atherosclerosis. They are associated with chronic and progressive stenosis of the arterial lumen rather than acute rupture. From a morphological point of view, they fall into three main categories: fibrocalcified plaques, healed plaque ruptures (HPR), and chronic total occlusions (CTO) (Figure 1.2) [7]. Fibrocalcified plaques are characterized by an abundance of dense connective tissue and extensive calcification, with minimal inflammatory infiltration. The ECM, composed mainly of collagen and proteoglycans, provides strong structural cohesion and limits the risk of rupture [7]. HPR are evidence of a successive repair process following previous ruptures or erosion [8]. Each healing episode results in the deposition of a fibrous layer rich in SMCs, collagen and proteoglycan matrix, covering the anterior necrotic core. This accumulation leads to a characteristic histological stratification, where successive layers of collagen-rich tissue and SMCs pile up, causing the arterial wall to condense and harden as the plaque matures. This process is closely linked to adaptive intimal thickening, where the progressive accumulation of these components in the internal layers inevitably results in the thickening of the vascular wall [9]. While this remodeling stabilizes the plaque, it severely reduces the luminal diameter, potentially leading to chronic ischemia [7]. CTO represent an advanced stage of atherosclerosis and are generally considered stable plaques. They are characterized by a complete obstruction of the arterial lumen by organized fibrous tissue, often with calcification. Unlike vulnerable plaques, CTO lack a large necrotic core and are not associated with acute rupture or thrombosis [7]. However, despite this stable phenotype, CTO are not benign. The occlusion prevents normal blood flow in the coronary artery, and although collateral vessels may form, they are often insufficient, frequently requiring intervention. CTO may also exhibit chronic inflammation and intraplaque neovascularization [7].

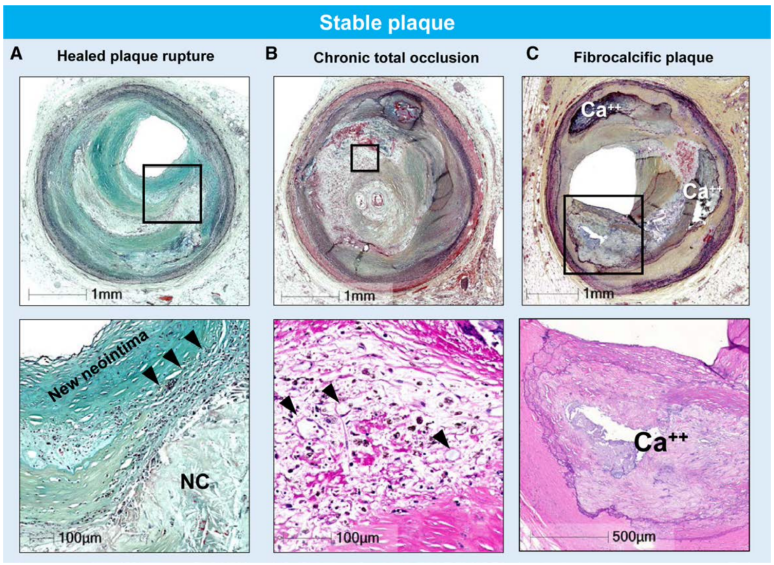


Figure 1.2: Representative examples of stable atherosclerotic plaques observed in histology, including A: healed plaque rupture, B: chronic total occlusions and C: fibro-calcified plaques. These images illustrate lesions characterized by a more structured tissue organization and increased stability compared to vulnerable plaques. Standard histological stains (Movat pentachrome and haematoxylin-eosin)[7].

Unstable plaques, also known as vulnerable plaques, include several morphological forms with a high risk of acute thrombotic events. They include thin-cap fibroatheromas (TCFA), ruptured plaques, erosive plaques, fissures, calcified nodules (CN), and intraplaque hemorrhages [7].

TCFA (Figure 1.3A) is the prototype of vulnerable plaque. It is characterized by a large necrotic core covered by a thin fibrous cap ($< 65\mu m$) infiltrated with macrophages and T lymphocytes. This cap contains few SMCs and a small amount of type I collagen, making it highly fragile. Plaque rupture (Figure 1.3D) is associated with complete fibrous cap disruption and an increased necrotic core size relative to the total plaque area (34% on average versus 23% in TCFA). Intraplaque hemorrhage (Figure 1.3B) contributes to rapid growth and structural degradation of plaques. Extravasated blood brings free cholesterol and iron, stimulating the formation of an extensive necrotic core and persistent inflammation. Plaque fissure (Figure 1.3C) has localized microtears in the cap, establishing partial communication between the lipid core and the arterial lumen. Although often clinically silent, these lesions mark an early stage of destabilization potentially leading to complete rupture.

Erosive plaques (Figure 1.3E) are characterized by a loss of the luminal endothelium, without rupture of the underlying cap. The lesion base, rich in proteoglycans, SMCs, and hyaluronan, creates an environment conducive to platelet adhesion. These lesions often lead to the formation of a non-occlusive thrombus, in the absence of clear rupture. Finally, CN (Figure 1.3F) are another type of unstable lesion, which is rarer (approximately 2 to 5% of sudden coronary deaths). They appear in areas of fragmented calcification, where protruding calcium deposits penetrate the lumen, triggering local thrombosis [7].

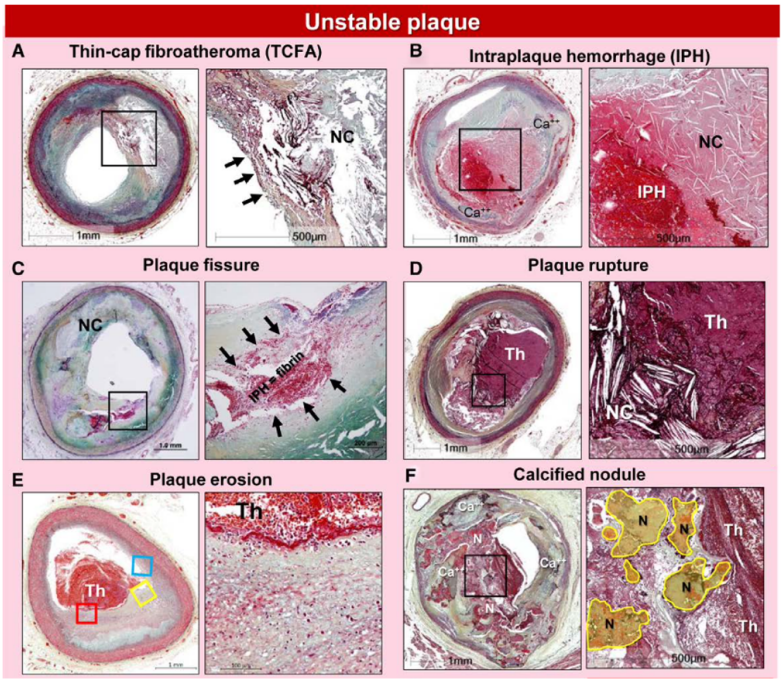


Figure 1.3: Representative examples of unstable atherosclerotic human plaques observed in histology, including A: thin-cap fibroatheroma, B: intraplaque hemorhage, C: plaque fissure, D: plaque rupture, E: plaque erosion, and F: calcified nodules. The images illustrate the diversity of plaque destabilization mechanisms associated with acute coronary syndrome [7].

1.2.2 Mechanisms of plaque destabilization and rupture

Plaque rupture occurs when the mechanical stress applied to the fibrous cap exceeds its breaking strength. This strength is mainly provided by the collagen content [1]. Macrophages play a central role in destabilization. In unstable plaques, macrophages adopt a pro-inflammatory phenotype and secrete pro-inflammatory cytokines [7]. They also release matrix metalloproteinases and other enzymes that

degrade collagen and the ECM, thereby weakening the fibrous cap and increasing the risk of rupture [5].

The rupture of a plaque exposes the highly thrombogenic contents of the necrotic core to the bloodstream, triggering a coagulation cascade that leads to the formation of a luminal thrombus [2, 5]. Partial or complete occlusion of the artery by this thrombus is the cause of acute cardiovascular events [7]. There are three main mechanisms of acute luminal thrombosis identified [7]. The first one is the plaque rupture (Figure 1.3D). This is the most common cause of myocardial infarction and sudden death. It is characterized by a discontinuity in the fibrous cap, exposing the necrotic core to the bloodstream [7]. The second one is plaque erosion (Figure 1.3E). This is responsible for approximately 30% of acute coronary syndromes (ACS) [10]. In this case, the endothelial layer is disrupted or absent, but the fibrous cap remains intact over the lipid core [2]. The last mechanism are CN (Figure 1.3F). It accounts for approximately 10% of lesions responsible for ACS [8]. It is defined by the presence of prominent, eruptive calcium deposits that break through the fibrous cap and protrude directly into the arterial lumen, triggering local thrombosis [7].

These acute events, whether caused by rupture, erosion, or CN, are the pathophysiological drivers of myocardial infarction, stroke, and sudden death [1, 7]. Identifying and managing unstable plaques and seeking to stabilize them are therefore fundamental to reducing cardiovascular morbidity and mortality [1].

1.3 Current therapeutic strategies

Stabilizing and regressing plaques are major goals of modern cardiovascular interventions [6]. The current strategy is based on managing risk factors (smoking, diabetes, hypertension) and the use of pharmacological and non-pharmacological interventions [2, 7].

Interventions aimed at modifying lipoproteins, particularly intensive LDL cholesterol reduction, are currently the most robustly proven strategy for inducing atherosclerotic plaque regression [2]. Statins are considered the first line of treatment for hyperlipidemia [7]. The high-intensity formulations significantly reduce atherosclerotic burden, both in percentage atheroma volume (PAV) and total atheroma volume (TAV) [2]. Beyond their lipid-lowering effect, they exert pleiotropic stabilizing actions, notably by improving endothelial function and reducing inflammation [7]. Their use slows the progression of PAV, promotes the formation of calcified plaque and reduces the appearance of high-risk plaques and

these effects translate into a significant reduction in cardiovascular mortality [6]. Proprotein convertase subtilisin/kexin type 9 (PCSK9) inhibitors, further enhance this action when added to statins: they powerfully lower LDL, further reduce PAV and TAV, increase the thickness of the fibrous cap, and decrease the lipid and inflammatory components of the plaque [2, 6]. Ezetimibe, used in combination therapy, has been shown to reduce PAV in some trials, although results are less consistent with regard to structural changes in plaque [2, 7].

Despite intensive LDL cholesterol lowering, a residual cardiovascular risk remains [2]. This residual risk is partly associated with persistent inflammation and elevated triglyceride levels, which has led to the development of therapies targeting these mechanisms. Icosapent ethyl has been shown to reduce atherosclerotic plaque burden in statin-treated patients with high triglycerides, likely through anti-inflammatory effects [2]. Similarly, colchicine, an established anti-inflammatory drug, has been associated with a reduction in major cardiovascular events [7].

Cardiometabolic risk management is an important component of plaque stabilization. Some glucose-lowering therapies have shown potential beneficial effects on atherosclerotic plaques [6]. For instance, certain agents such as pioglitazone, metformin, or semaglutide have been associated with plaque stabilization or regression, likely through metabolic and anti-inflammatory mechanisms. However, these effects are not uniform across all drug classes, highlighting the need for careful therapeutic selection [6].

Finally, lifestyle interventions remain an essential pillar [2]. An intensive approach combining a low-fat vegetarian diet, physical activity, and stress management has demonstrated a gradual reduction in coronary stenosis in preliminary studies [2].

Chapter 2

Experimental mouse models for atherosclerosis

The mouse has become the predominant species for the experimental study of atherosclerosis due to its rapid reproduction, ease of genetic manipulation and ability to monitor atherogenesis over a reasonable period [1]. This relevance is supported by the fact that mice and humans share approximately 95% of their protein-coding genes [4]. However, it is important to note that no inbred mouse strain develops atherosclerosis spontaneously [5].

In mice, the lipid profile differs from that of humans, which contributes to their natural resistance to atherosclerosis. About 80% of the circulating cholesterol in mice is transported by HDL, known for their anti-atherogenic effects [4, 5]. Conversely, in humans, nearly 75% of cholesterol is contained in LDL or VLDL, which are much more atherogenic [5]. Mice also lack cholesteryl ester transfer protein (CETP), a key enzyme in humans that transfers cholesterol esters from HDL to LDL/VLDL, further enhancing this metabolic difference [3]. The locations of atherosclerotic plaques also differ between species. In mice, lesions appear mainly in the aortic root, the curvature of the aortic arch and bifurcation areas such as the brachiocephalic arteries or the carotids [1]. In contrast, in humans, plaques develop primarily in the coronary arteries and carotids, which frequently leads to myocardial infarction or stroke, very rare events spontaneously in mice [1, 3].

Despite these metabolic and anatomical differences, murine models remain highly relevant because the fundamental composition and development of atherosclerotic plaques are remarkably similar to those in humans. Both species share key pathological features, such as lipid accumulation, foam cell formation, and the

development of necrotic cores and fibrous caps. However, nuances exist. The most significant discrepancy lies in the immune response. For example, T-cells are far more prevalent in human plaques than in murine lesions [3, 5].

Furthermore, while the structural components are shared, traditional murine plaques often exhibit greater stability than vulnerable human plaques. For example, unstable human plaques are characterized by a TCFA, whereas in mice, this capsule is generally thicker and more resistant [3]. The necrotic core, although present in both species, is often less voluminous in murine lesions than in advanced human plaques [1, 3].

Finally, the major complication observed in humans, plaque rupture leading to acute thrombosis, is rare in mouse models [1, 3]. Mouse plaques almost never rupture spontaneously to the point of causing an infarction, which limits the direct transposition of murine observations to human [3]. Given the mouse's natural resistance to atherosclerosis, hypercholesterolemia must be induced by modification or inactivation of key genes regulating lipid metabolism [5].

2.1 The apolipoprotein E deficient model ($ApoE^{-/-}$)

The $ApoE^{-/-}$ is one of the pillars of atherosclerosis research. Apolipoprotein E (ApoE) normally plays an essential role by acting as a ligand for LDL receptors, thereby enabling hepatic clearance of triglyceride-rich lipoproteins, such as chylomicrons and VLDL [3]. Introduced in 1992, $ApoE^{-/-}$ mice have quickly gained a central place in the field [1]. The inactivation of the ApoE gene leads to an inability to effectively remove lipoprotein residues, which profoundly modifies lipid metabolism [3]. These mice indeed develop massive hypercholesterolemia even when they are fed a standard diet [3]. Unlike the human situation, where cholesterol circulates mainly in LDL particles, ApoE cholesterol is mainly transported by triglyceride-rich lipoproteins, notably VLDL and LDL [3, 5].

On the vascular plane, $ApoE^{-/-}$ mice spontaneously develop the full range of atherosclerotic lesions, from lipid striations to complex fibrous plaques, with accelerated progression in the presence of a high fat diet [3]. The lesions appear preferentially in the aortic root and the aortic arch, areas subject to significant hemodynamic stress, which partly reflects the localizations observed in humans [5]. Similarly, in humans, atherosclerotic plaques develop predominantly at arterial sites exposed to disturbed flow and elevated hemodynamic stress [11].

However, this model has some limitations. The atypical lipid profile, dominated by VLDL rather than LDL, differs significantly from human physiology. Moreover, ApoE$^{-/-}$ also participates in processes not related to lipids, such as inflammation or immunity, which can complicate the interpretation of the results obtained and limit direct transposability to human mechanisms [3].

2.2 The low-density lipoprotein receptor-deficient model (LDLr$^{-/-}$)

The low-density lipoprotein receptor (LDLR) plays an essential role in the clearance of circulating LDL cholesterol. LDLr$^{-/-}$ mice, introduced in the early 1990s, constitute the second most widely used genetic model in research. Their LDLR deficiency partially recapitulates key aspects of human familial hypercholesterolemia Under normal diet, these mice develop moderate hypercholesterolemia [3]. Unlike ApoE$^{-/-}$, cholesterol accumulates mainly in the form of LDL cholesterol which is a major advantage, as the lipid profile then becomes more comparable to that observed in humans [3, 5]. The development of atherosclerotic plaques is however slower than in the ApoE$^{-/-}$ model. The onset of significant damage often requires a prolonged Western diet [3]. The plaques then form gradually, with a dynamic that partially reflects human physiopathology but remains less aggressive [5]. This model nevertheless presents an important limitation. The absence of the LDLR makes these mice less suitable for evaluating therapies that rely on increasing the expression or activity of LDLR, such as statins or PCSK9 inhibitors [3, 5]. Nevertheless, it is important to note that statins can still be utilized in this model if the research objective is to assess other effects, such as their anti-inflammatory properties, which occur independently of the LDLR [3].

2.3 ApoE3-Leiden transgenic model

The transgenic ApoE3-Leiden model was developed to best reproduce human lipid metabolism. These mice express the human variant ApoE3-Leiden, which has a reduced affinity for the LDLR, and also possess the human transgene encoding [3]. The presence of CETP is particularly important because this enzyme plays a central role in humans by transferring cholesterol esters from HDL to LDL and VLDL [3]. This model is widely used to test new lipid-lowering agents. It is particularly relevant to evaluate therapies targeting LDLR, CETP or HDL regulation, since endogenous ApoE$^{-/-}$ and the LDLR remain functional [3, 5].

2.4 The adeno-associated virus stereotype 8 mediated PCSK9 expression (AAV8-mPCSK9) model

To avoid the limitations of traditional models, a method increasingly used in current research is the induction of hypercholesterolemia via a single injection of an adeno-associated viral vector expressing a gain-of-function form of PCSK9 [1]. This approach leads to the rapid degradation of hepatic LDLR, resulting in sustained hypercholesterolemia and the rapid induction of atherosclerosis [1, 3].

The biological and practical advantages of this model over historical germline strains, such as the ApoE$^{-/-}$ or LDLr$^{-/-}$, are significant. From a logistical standpoint, while generating colonies of compound mutant mice through crossbreeding is a costly and time-consuming process (up to two years), the AAV8-mPCSK9 model allows for the immediate induction of atherosclerosis in any existing genetically modified strain without the need for complex intercrossing [12]. Furthermore, unlike germline knockouts which are subject to developmental compensations from birth, the AAV8-mPCSK9 model allows for the induction of atherosclerosis in "wild-type" adult mice. This ensures that the disease develops within a mature, non-modified immune system, providing a more accurate representation of the inflammatory environment seen in human patients [1].

Other studies, including the work of Goettsch et al. (2016), confirms that this model produces complex, heterogeneous plaques. Specifically, it has been demonstrated that mPCSK9 injection in mice fed a high-fat, high-cholesterol diet for 15 to 20 weeks induces significant vascular calcification, with alkaline phosphatase activity and calcium deposits similar to those observed in LDLr$^{-/-}$ [12]. However, it is important to note that while this model reflects the pathological diversity and calcification found in clinical cases, it does not spontaneously result in plaque rupture. By utilizing this model, it becomes possible to study the disease's progression and mineral deposition in a physiological context that avoids the confounding metabolic factors often associated with earlier genetic models [12].

Despite these advantages, several limitations must be considered when utilizing the AAV8-mPCSK9 model. First, inter-individual variability in hypercholesterolemia and lesion progression often requires post-mortem validation of viral vector efficiency [3]. Second, compared to traditional knockout strains, these mice exhibit a longer latency for mineralization and develop less extensive lesions, predominantly restricted to the aortic arch [12, 13]. Finally, consistent with most

traditional murine models, the AAV8-mPCSK9 framework does not spontaneously result in plaque rupture or acute thrombus formation, which remain the primary drivers of clinical events in human [3].

Chapter 3

Imaging techniques for plaque characterization in mice models

3.1 In vivo imaging techniques

3.1.1 Ultrasound biomicroscopy (UBM)

UBM is today a widely used technique for longitudinal and non-invasive monitoring of atherosclerosis in mice [14]. Unlike conventional ultrasound, it uses high-frequency transducers, typically between 30 and 50 MHz [14, 15]. This high frequency allows obtaining a spatial resolution of the order of 30 to 50 µm. Such a resolution is necessary to observe the very small vascular structures of rodents, whose dimensions are often millimetric [15].

Several studies have shown that this technique allows to directly visualize certain regions of the aorta in mice. For example, in $LDLr^{-/-}$, the UBM allows real-time imaging of the anatomy of the ascending aorta and the aortic arch [14, 15]. From these images, different measurements can be carried out. In particular, it is possible to measure the thickness of the atherosclerotic plaque. In some studies, the values obtained by UBM show a very strong correlation with those measured in histology, with a coefficient that can reach $r = 0.90$ [15]. Short-axis imaging also allows the delineation of the lesion surface, which provides a reliable way to track disease progression over time [14]. Finally, UBM can be used to observe vascular remodeling, for example the increase in the external diameter of the vessel or the thickening of the intima-media complex, sometimes even before a significant stenosis is visible [14].

Beyond the morphological aspect, UBM can also provide functional information when associated with the Doppler mode [15, 16]. This combination allows the measurement of blood flow velocity and identification of turbulence areas, especially in regions where plaques occur frequently, such as the aortic sinus [11, 16, 17]. This type of analysis is important to better understand vascular biomechanics phenomena associated with the development of atherosclerosis [11]. One of the main advantages of UBM is its non-invasive nature. It is therefore possible to perform several measurements on the same animal over time, which reduces the number of mice needed for experimental studies [15, 18]. However, the technique also has some limitations. First, the quality and accuracy of measurements strongly depend on the operator's experience and the angle of incidence of the ultrasonic beam [14, 15]. Then, despite its good resolution, the UBM does not always allow to observe in detail the internal microstructure of the plaque, such as the fibrous cap or the micro-calcifications [17, 19]. Finally, access to certain anatomical regions remains difficult. For example, the study of the descending thoracic aorta is often limited by the presence of air in the lungs, which restricts imaging mainly to the root and aortic arch [15, 17].

3.1.2 Magnetic resonance imaging (MRI)

MRI is distinguished by its excellent soft tissue contrast, its non-invasiveness and the absence of ionizing radiation [19]. It allows direct visualization of the arterial wall and not just the vessel lumen, which is crucial for observing positive remodeling, common in early stages of atherosclerosis [17, 18]. Owing to different weights (T1, T2), the MRI distinguishes the components of plaque: the lipid nucleus, the fibrous cap and intra-plaque hemorrhage. In animal models, notably ApoE$^{-/-}$, MRI is valuable for longitudinal tracking of plaque progression or regression. However, the small size of the arteries requires very high field equipment and precise management of cardiac and respiratory movements [20].

MRI offers excellent tissue contrast, direct visualization of positive remodeling and accurate plaque characterization, while remaining non-invasive [17]. Its limitations include a long acquisition time, insufficient resolution for microstructures, high cost and certain technical constraints for imaging coronary arteries and the aortic root [17–21].

3.1.3 Positron emission tomography (PET)/Single photon emission computed tomography (SPECT)

PET and SPECT are molecular imaging techniques that allow the study of the biological activity of atherosclerotic plaques, beyond their simple morphology. These techniques are studied in the context of atherosclerosis due to their high sensitivity and quantification capability [22]. In mice, molecular imaging represents a major technical challenge due to the small size of vascular structures (the murine aorta having a diameter of about 1 mm) and the low density of target cells within the lesions [22].

The most widely used tracer is fluorine-18 fluorodeoxyglucose (18F-FDG), an analogue of glucose captured by cells with high metabolic activity, particularly activated macrophages present in inflammatory plaques [23, 24]. Studies on $ApoE^{-/-}$ subjected to a high-fat diet demonstrated an aortic uptake of 18F-FDG increasing proportionally with age and plaque progression [25]. However, its use for imaging the coronary arteries is limited by the strong physiological uptake of the myocardium [22]. Because the heart muscle naturally consumes a large amount of glucose, it absorbs the tracer intensely, creating a high background signal (false positives) that overlaps and masks the much weaker signal from the adjacent coronary plaques. This issue is further compounded by a lack of cell specificity [22].

Another major tracer is the fluorine-18 sodium fluoride (18F-NaF), which targets areas of active microcalcification within plaques [23, 26]. Unlike 18F-FDG, 18F-NaF is not captured by the myocardium, making it an excellent tracer for assessing coronary arteries [23]. In mice, studies have also demonstrated the usefulness of this tracer for identifying atherosclerotic lesions, particularly in pulmonary arteries where it accumulates significantly over time [26]. In order to improve biological specificity, new PET tracers have been developed to target specific processes such as macrophagic inflammation, hypoxia or angiogenesis [10, 23]. Although promising, these tracers remain mostly at the research stage and their clinical use remains limited.

SPECT has lower sensitivity and spatial resolution than PET [22]. However, SPECT is often superior to PET to target the tiny arterial plaques of the mouse. Thanks to the use of specific collimators (multi-pinhole) offering a geometric magnifying effect, microSPECT systems reach sub-millimetric spatial resolutions [22]. Several SPECT tracers have been developed to target apoptosis, inflammation or endothelial activation, thus contributing to the study of biological mechanisms involved in the progression of atherosclerosis [22]. Despite their strong potential,

PET and SPECT have technical limitations, particularly related to their spatial resolution, which complicates the imaging of small structures in animal models. These modalities are therefore most often combined with anatomical imaging techniques, such as computed tomography (CT) or MRI, in order to precisely locate the molecular signal [19, 23].

3.1.4 Photoacoustic imaging (PAI)

PAI represents a growing hybrid biomedical modality, suited for the exploration of atherosclerosis on mice models. This technique merges the strengths of two techniques: the spectroscopic selectivity and high contrast optics of optical imaging, and the ultrasonic tissue penetration capability of the echography [19]. The process is based on the irradiation of tissues by laser pulses of the order of nanosecond, without recourse to ionizing radiation. Photons are selectively captured by specific molecular targets, or chromophores. This energy absorption induces a local thermal micro-elevation, triggering a transient thermoelastic expansion. The resulting relaxation emits acoustic waves, which are captured by high-frequency piezoelectric sensors in order to model a high-resolution structural mapping [19, 27].

In the context of the study of atherosclerosis in mice, the applications of this technology are divided into two main methodological approaches. The first one exploits endogenous signals by targeting natural absorption properties of tissues in the near infrared window (between 1200 and 2000 nm) [27]. This strategy allows the direct in vivo quantification of lipid load and collagen content, thus providing an accurate assessment of necrotic nucleus size and degree of plaque fibrosis [27]. The second approach relies on exogenous molecular imaging via targeted contrast agents to refine phenotypic characterization. Specific fluorescent probes make it possible to map macrophage infiltration and the expression of receptors linked to the accumulation of oxidized lipids, two key markers of plaque vulnerability (Figure 3.1) [27, 28]. At the same time, the use of macromolecular dyes such as Evans blue allows early detection of endothelial permeability abnormalities, which are characteristic of areas favorable to atheroma development (Figure 3.1) [27].

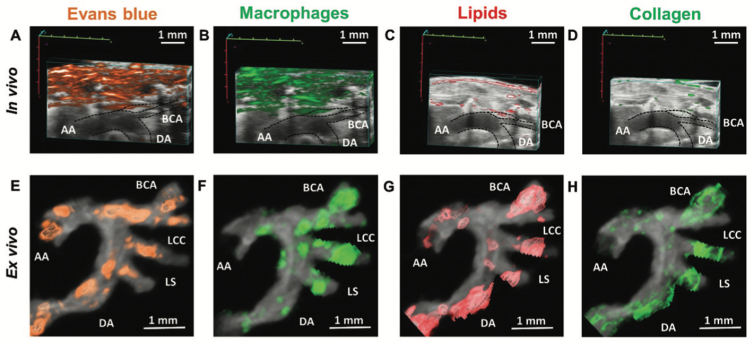


Figure 3.1: Photoacoustic imaging of mouse atherosclerotic lesions. Representative images of the unmixed photoacoustic signal of Evans Blue, macrophages, lipids, and collagen, respectively, in 3D in vivo scans of a mouse bearing advanced lesions (panels A-D). Representative images of the unmixed photoacoustic signal of the above-mentioned molecules or dyes, in 3D ex vivo scans of mice displayed in (A–D) (panels E-H). (Adapted from [27]).

Despite this potential, the application of PAI in small animals remains subject to biophysical and technical barriers. The first obstacle concerns the depth of penetration, as attenuation and light scattering limit efficient examination to superficial vascular structures [19]. If the PAI is particularly effective for analyzing carotid arteries or the brachiocephalic trunk, located between 2 and 5 mm deep, it struggles to image lesions lodged deeper in the thoracic cage [27]. The second challenge lies in physical interference and the complexity of signal processing. The crossing of surrounding bone structures causes phase distortions on the acoustic waves, while the strong absorption of circulating hemoglobin creates an omnipresent background noise which requires complex separation algorithm to isolate the signal of interest [19].

In summary, in vivo imaging techniques offer valuable information on the anatomy, composition and biological activity of atherosclerotic plaques. UBM and MRI can assess the vascular structure and progression of plaques in a non-invasive way, while PET and SPECT provide insights into inflammation, active calcification, and other molecular processes. PAI further enhances these capabilities by merging ultrasound penetration with optical spectroscopy, allowing for the non-invasive tracking of lipid load, fibrosis, and targeted inflammatory markers. However, despite these advances, in vivo imaging remains limited by its resolution and depth of penetration. These constraints make it difficult to accurately analyze the overall structure, complete composition, and total volume of the plaques in order to asses the risk that they represent. These limitations justify the use of ex-vivo approaches, which offer

higher spatial resolution and allow for better tissue differentiation.

3.2 Ex vivo imaging techniques

3.2.1 Classical two dimensions (2D) histology

3.2.1.1 General principles of histological analysis

Classical 2D histology is the study of tissue at the microscale. It allows a fine analysis of the cellular and tissue components of atherosclerotic plaques, with high resolution. Therefore, it is widely used for the study of atherosclerotic lesions in animal models.

The classical 2D histological preparation is based on a rigorous protocol aimed at preserving tissue architecture. After dissection of the heart and vessels, tissues are rinsed to remove blood, then fixed with formalin 10% or paraformaldehyde [29]. For the analysis of the aortic root region in mice, the heart is usually perfused with phosphate-buffered saline (PBS) to completely eliminate residual blood cells before attachment. The collected tissues are then fixed in 4% paraformaldehyde for 24 to 48 hours [5]. This step is essential to maintain cell integrity and the structure of the ECM. The samples are then included in a solid medium to allow for their cutting. Paraffin embedding is mainly used for general morphological analysis, as it offers superior preservation of tissue architecture. However, a major downside of this technique is that the required dehydration stages unfortunately dissolve lipids [9]. Cryosectioning (frozen sections) is a good solution to this problem as it allows the visualization of lipids [30]. That is why the blocks are then frozen and sectioned using a cryostat, with thicknesses ranging from 5 µm for paraffin tissues [5] to a thickness generally varying between 6 to 12 µm for freezing sections [30, 31]. Several colorations and marking techniques are used to characterize the components of the plaques. Hematoxylin and eosin staining allows the evaluation of general morphology and cell organization [30, 32]. The Movat pentachrome provides a detailed differentiation of vascular wall constituents, including collagen, elastic fibers and proteoglycans [9]. Neutral lipids are visualized using Oil Red O or Sudan IV on frozen sections [30]. Collagen can be quantified using Sirius Red, often analyzed under polarized light [9, 32]. Finally, immunohistochemistry allows the identification of specific cell populations, such as macrophages or SMCs, using targeted antibodies [32, 33].

3.2.1.2 Classical 2D histology for the characterization of atherosclerosis in mouse models

Classical 2D histological analyses focus on the aortic root, the aortic arch and the brachiocephalic artery, which are preferential sites for plaque development in mice [34]. To ensure a representative volumetric estimation across the aortic sinus while accounting for spatial heterogeneity, the plaque area is traditionally measured over serial sections per animal, typically spaced by 50 to 100 µm [5]. Specifically, a standardized protocol optimized for the aortic root relies on a 4 sections analysis spanning a total distance of 150 µm from the point where the aortic valve leaflets open [5]. Classical 2D histology is widely used to describe and categorize the temporal progression of atherosclerotic lesions based on the American Heart Association guidelines [5]. In the early stages, mild lesions (Types I and II) known as fatty streaks are observed (Figure 3.2). They are mainly composed of macrophages loaded with lipids accumulated in the subendothelial space [9, 30]. Type I lesions represent early fatty streaks containing a maximum of 10 foam cells within the intima, whereas Type II lesions are regular fatty streaks showing more than 10 foam cells [5]. At an intermediate stage, the lesions become thicker and multicellular and the foam cells begin to extend into the media, while the plaque starts to be covered by a fibrous cap (Figure 3.2 Type III) [5]. In advanced stages, plaques progress into severe lesions (Figure 3.2 Types IV and V) with a highly complex organization. Type IV represents moderate plaques characterized by extensive media infiltration and fibrosis, although the general architecture of the vessel remains intact [5]. Type V represents severe plaques where the media is heavily damaged, leading to a breach in the elastic lamina [5]. These severe lesions develop a necrotic core made of cellular debris, cholesterol crystals, and mineralization, covered by a fibrous cap rich in collagen and SMCs [4, 30].

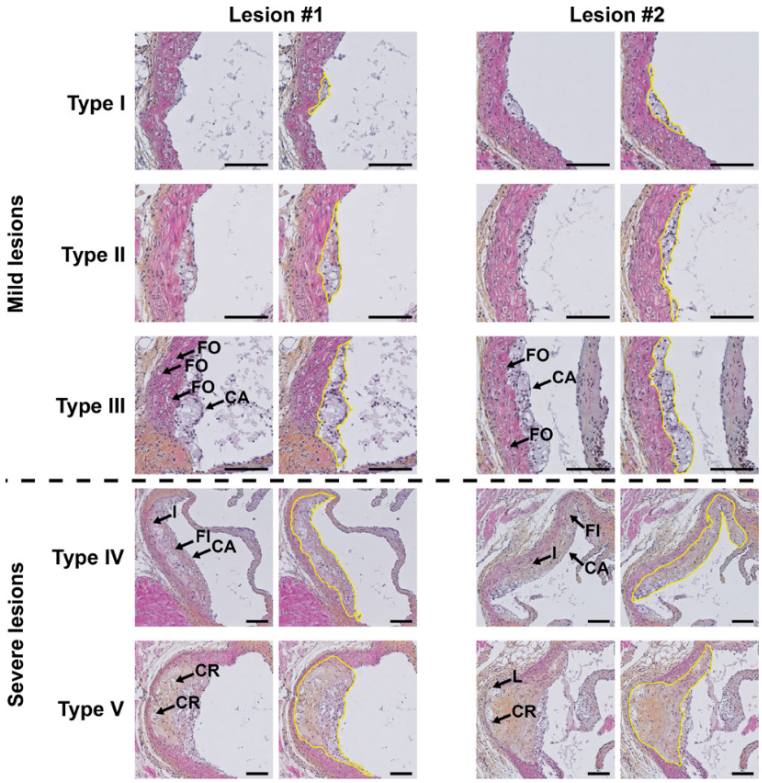


Figure 3.2: Histological classification of atherosclerotic lesion severity in the mouse aortic root. Representative images of sections stained with hematoxylin–phloxine–saffron. Lesions are categorized into mild (Types I–III) and severe (Types IV–V) plaques. Yellow outlines delineate the circumference of each lesion. Abbreviations indicate: FO = foam cells extending into the media; CA = fibrotic cap; I = infiltration into the media; FI = fibrosis; L = breach in the elastic lamina; CR = cholesterol crystals. Scale bars = 200 µm. (Adapted from [5]).

3.2.1.3 Limitations of classical 2D histology for plaque analysis

Despite its status as a gold method, classical 2D histology has several major limitations. Calcification represents a major obstacle for the histological analysis of the structure of atherosclerotic plaques. Two main reasons explain this difficulty: the technical constraints related to sample preparation and the limits of 2D analysis for a complex 3D phenomenon.

Hard calcium deposits within soft tissues complicate standard histological preparation. To obtain fine sections observable under the microscope, it is often necessary to carry out a chemical decalcification. This process dissolves the minerals, which

prevents analysis of the plaque's native mineral density or composition. Even with this step, or on frozen samples, the mechanical cutting of heterogeneous tissues can cause tearing, wrinkles, or tissue loss, thus altering the structural integrity of the plaque [35]. Beyond these physical constraints, the primary challenge of conventional histology lies in sampling bias: a single cross-section, or even a series of spaced sections, cannot faithfully represent the longitudinal and volumetric heterogeneity of a plaque.

Secondly, classical 2D histology relies on 2D slices, which makes it difficult to assess calcifications and lipid distributions, which are 3D and heterogeneous. It does not allow capturing the complete spatial distribution, the exact shape, or the connectivity of calcified particles. This lack of spatial continuity constitutes a critical issue when quantifying the total atherosclerotic load or localizing unpredictable sites of vulnerability that might be situated between two cutting planes. Classical 2D histology can nevertheless detect microcalcifications (0.5 to 15 µm) thanks to specific stains (like Von Kossa or Alizarin Red) [7].

In summary, calcification complicates classical 2D histological analysis because it often requires the destruction of the mineral target, and 2D analysis does not account for the 3D complexity of the deposits nor the volumetric continuity of the lesion. These limitations justify the use of ex vivo 3D techniques to characterize both calcification and soft tissues, while maintaining the overall structure of the plaque across the entire vessel volume.

3.2.2 X-ray microfocus-computed tomography (microCT) and CECT for plaque characterization

3.2.2.1 X-ray microfocus-computed tomography

The microCT is a non-destructive 3D imaging technique based on the use of X-rays. Its principle is based on the differential attenuation of the X-ray beam as it passes through the sample, an attenuation that mainly depends on the density and atomic composition of the tissues. During acquisition, the system generates a series of cross-sectional images (radiographs) obtained at different rotation angles, which are then digitally reconstructed to form a complete 3D volume of the sample [36]. Two imaging modes can be distinguished. The absorption mode, most commonly used, directly exploits differences in X-ray attenuation between tissues [37], and the phase contrast mode, more specialized and generally limited to synchrotron installations, relies on the beam phase shift and allows to improve the contrast of weakly absorbent tissues [38].

One of the main advantages of microCT is its high spatial resolution, which makes it particularly suitable for imaging small animals such as mice. In ex vivo conditions, voxel sizes of the order of micrometers can be reached, largely exceeding the performance of clinical techniques or in vivo MRI [38]. Finally, another important advantage is that microCT is a non-destructive technique, allowing the preservation of the sample and enabling subsequent complementary analyses such as histology or molecular assays [39].

MicroCT is particularly well suited for the study of vascular calcifications, as mineralized tissues exhibit a strong attenuation from X-rays. This property confers high natural contrast to calcium deposits, allowing their detection and quantification without recourse to additional contrast agents [37]. This property enables the detection and quantitative analysis of calcium deposits across multiple spatial scales, from early microcalcifications to larger calcified regions [40]. Thanks to this level of precision, one study has proposed a refined classification of calcifications at macro-, meso-, and micro-scales, allowing the detection of early calcification onsets that remain invisible using conventional clinical imaging techniques [40]. In addition, microCT enables 3D characterization of calcification morphology, such as punctate, fragmented, or sheet-like structures, as well as quantification of calcified volume and mineral density within the plaque [7]. While this capability is exploited for the study of calcified heart valves in mice, particularly in models of aortic stenosis [29], a significant gap remains in the simultaneous characterization of both valvular mineralized deposits and surrounding soft tissue components within the same aortic root region, including the aortic sinus. Work has shown a close correlation between the calcium load measured by microCT and the severity of the stenosis, highlighting the relevance of this technique for the study of calcified valvular pathologies [29].

Despite these advantages, standard microCT, especially when used in absorption mode, remains limited in its ability to differentiate soft tissues. Indeed, the different non-mineralized components of atherosclerotic plaque, such as the arterial wall, lipid regions or fibrous tissues, have very similar and low X-ray attenuation coefficients [41]. This proximity of attenuation strongly limits the intrinsic contrast between these tissues and makes their distinction difficult, representing a major hurdle for identifying the necrotic core or the fibrous cap without staining. In in vivo conditions, these limitations are accentuated by additional technical constraints. The dose of radiation must be strictly controlled to avoid deleterious effects on the physiology of the animal, which imposes a compromise between spatial resolution and safety [19].

However, despite its remarkable performance for volumetric analysis and calcification quantification, the standard microCT remains limited for the characterization of plaque soft tissues, which led to the development of approaches based on the use of dedicated contrast agents.

3.2.2.2 Contrast-enhanced microCT

CECT is based on enhancing the contrast of soft tissues, which naturally exhibit low X-ray attenuation and are therefore difficult to distinguish in standard microCT [37]. To overcome this limitation, CECT uses specific contrast agents, capable of increasing the attenuation of X-rays within non-mineralized biological structures [37]. The principle of the technique is to impregnate the sample with contrast agents rich in high atomic number elements, such as iodine, tungsten or hafnium. These agents, referred to as contrast-enhancing staining agent (CESA), diffuse passively in ex vivo tissues and are distributed according to their physico-chemical interactions with the tissue components. Their presence locally increases the attenuation of X-rays, thus making visible previously indistinguishable structures, such as the proteins in the arterial wall, non-calcified components of atherosclerotic plaque or surrounding muscle tissues [37, 38, 41]. Despite the potential of CESAs, the literature currently lacks standardized protocols for the precise segmentation of the aortic root in modern induction models like AAV8-mPCSK9 (Section 2.4), where the convergence of valves and coronary ostia complicates the volumetric analysis. Different types of CESAs have been developed and are chosen according to the targeted biological application. Iodinated solutions are widely used for their relatively homogeneous diffusion and ease of use [37]. Phosphotungstic acid (PTA) has been claimed to have a particular affinity for collagen- and fibrin-rich tissues, which makes it particularly interesting for the study of the ECM and fibrous components of plaques [29]. More recently, polyoxometalate (POM) based agents have been introduced in order to achieve high soft tissue contrast while preserving sample integrity, thus enabling detailed 3D analyses [41].

Like microCT, the CECT allows a complete 3D visualization of the plaque and vessel architecture [42]. The sample can be explored in any spatial orientation, without altering its overall structure, which facilitates morphological and volumetric analysis of lesions [37]. A major advantage of the CECT is its ability to simultaneously characterize soft tissues and mineralized tissues [37]. While standard microCT provides a high natural contrast for calcifications, the addition of CESAs also allows to distinguish the arterial wall, vascular lumen and the different components of plaque [43]. This approach allows a precise and coherent segmentation of all the vascular structures in the same 3D volume [37]. The CECT also benefits from a very high spatial resolution. Current microCT ex vivo systems can reach voxel

sizes in the micrometer range, typically between 3.5 and 6 µm [29], with identical isotropic resolution in all 3D [38, 41]. Although this resolution, close to that of classical 2D histology allows the visualization of fine microstructural details, it may still be insufficient to resolve the thinnest vulnerable features of murine plaques, which can measure only a few micrometers.

In the atherosclerotic mouse, microCT is a particularly powerful tool for 3D and quantitative analysis of vascular lesions, especially when it comes to assessing the atherosclerotic burden and associated calcification [44]. Unlike classical 2D histology, limited to 2D sections, microCT and CECT can provide a global and continuous view of the disease along the vascular tree [44]. Quantitatively, microCT allows to accurately measure the total volume of the plaque, the intimal surface reached and the maximum thickness of the lesions on the entire aorta (Figure 3.3) [39]. However, the vast majority of validated studies focus on the ApoE$^{-/-}$, leaving a significant characterization gap for the AAV8-mPCSK9 model, which lacks high-resolution 3D reference data. Several studies conducted in ApoE$^{-/-}$ mice have shown an excellent correlation between the plaque volumes measured by microCT and those obtained by conventional histology, thus validating the robustness of this approach for assessing atherosclerotic burden [44]. The analysis allows to distinguish vascular lumen, arterial wall and pathological areas. This approach allows the calculation of global parameters, such as the ratio of plaque volume to aortic volume, and facilitates longitudinal comparisons or between experimental groups [44].

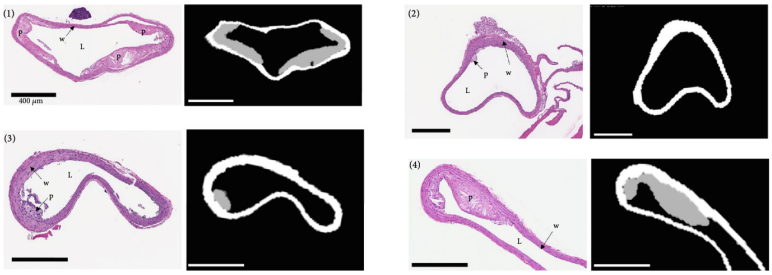


Figure 3.3: Representative paired histological (left) and microCT (right) sections illustrating the agreement between imaging modalities. p: plaque; L: lumen; w: wall; scale bar = 400 µm. (Adapted from [44]).

The CECT is used for both quantitative and qualitative analysis of atherosclerotic lesions in mice, especially under ex vivo conditions to maximize spatial resolution and tissue contrast [44]. This approach allows for a comprehensive 3D assessment of plaques across the entire arterial tree, which is a major advantage over classical 2D

histology. Thanks to the use of suitable CESAs, CECT allows precise volumetric segmentation of vascular lumen, arterial wall and plaque itself [38]. For example, CESAs like PTA increase the contrast of fibrous tissues, facilitating the distinction between healthy wall and the plaques [44]. It then becomes possible to reliably measure the total volume of the plaque, the lesion surface or even the degree of stenosis over the entire length of the aorta, and no longer only on isolated sections [44]. Yet, most current CECT applications focus on isolated segments of the aorta, often failing to maintain the heart's intact anatomy. This loss of context is problematic for studying the aortic root, where the 3D geometry is the primary driver of plaque localization and vulnerability. Beyond global quantification, the CECT also allows analyzing the organization of the arterial wall [43]. This visualization of elastic fibers and collagen within the media is particularly useful for studying vascular remodeling associated with atherosclerosis progression.

Although high-resolution CECT is most often used as a terminal technique, it is a particularly powerful tool for comparing cohorts of animals at different stages of the disease. Studies conducted on atherosclerotic mouse models have shown a gradual increase in plaque volume and lesion area with age, well correlated with classical histopathological scores [44]. Finally, CECT allows the detection of early stages of atherosclerosis, including intimal thickening and positive arterial wall remodeling, before any significant reduction in vascular lumen [20]. These phenomena, difficult to assess reliably in classical 2D histology, can be quantified precisely in 3D. In this context, the CECT can be used as an ex vivo method to validate the efficacy of experimental treatments or to compare the results of other in vivo imaging techniques, providing a detailed and quantitative anatomical description of lesions [44]. Nevertheless, the lack of automated and optimized segmentation tools for the aortic sinus in the AAV8-mPCSK9 model prevents this technique from reaching its full potential as a high-throughput diagnostic tool in preclinical research.

Chapter 4

Problem statement, general aim and objectives

The quantitative and structural characterization of atherosclerotic plaques in preclinical research is essential for understanding the mechanisms of lesion progression, stabilization, and vulnerability. Over the past decades, traditional inbred mouse strains, such as ApoE$^{-/-}$ and LDLr$^{-/-}$ models, have served as the historical pillars for studying atherosclerosis. However, these germline mutation models are increasingly associated with significant logistical and biological constraints. Generating compound mutant colonies through genetic crossbreeding is a costly, complex, and time-consuming process. Furthermore, germline knockouts are subject to developmental compensations from birth, altering the native systemic physiology.

To overcome these historical limitations, the induction of hypercholesterolemia via a single injection of an adeno-associated viral vector expressing a gain-of-function mutant of PCSK9 (AAV8-mPCSK9) in adult mice has emerged as a powerful alternative. By inducing the rapid degradation of hepatic LDL receptors, this modern model enables the immediate and highly aggressive development of complex, heterogeneous atherosclerotic plaques in any existing genetically modified or wild-type adult strain, ensuring a mature and non-modified immune system that closely reflects human inflammatory kinetics.

Despite the clear practical and biological advantages of the AAV8-mPCSK9 model, establishing its full diagnostic and analytical potential is heavily hindered by the limitations of conventional ex vivo characterization techniques. Classical 2D histology remains the historical gold standard for evaluating lesion composition, providing high cellular resolution for identifying necrotic debris and fibrous compo-

nents. Nevertheless, conventional histology is inherently destructive, labor-intensive, and highly susceptible to severe sampling bias. Because it relies on physically cutting thin, isolated cross-sections spaced along the vessel, 2D histology cannot faithfully capture the continuous 3D volumetric heterogeneity of a plaque. Crucially, the presence of hard calcium deposits embedded within soft pathological walls represents a major physical obstacle during sectioning, frequently causing severe tearing, micro-wrinkles, or complete tissue loss. To mitigate this damage, samples must undergo chemical decalcification prior to embedding, a process that inherently dissolves the native mineral target and completely prevents the preservation, localization, and dense assessment of the calcified phase. Conversely, conventional microCT excels at non-destructively resolving hyper-dense mineralized structures in 3D due to their strong natural attenuation properties. However, standard microCT absorption imaging exhibits a major limitation regarding soft vascular structures, as non-mineralized components like the healthy arterial wall, the lipid-rich necrotic core, and the protective fibrous cap share virtually identical and low X-ray attenuation coefficients, leaving them completely invisible and unclassifiable without additional contrast enhancement.

To bridge this critical characterization gap, CECT has recently emerged as a highly promising solution. By impregnating biological tissues with non-destructive macromolecular CESAs, such as hafnium-substituted Wells-Dawson 1:2 polyoxometalate (Hf-WD POM 1:2), CECT can artificially amplify the electron density of soft tissues according to their local macromolecular density while preserving the architectural integrity of the sample. However, a major technological and methodological milestone remains to be achieved regarding spatial resolution. While CECT frameworks have shown great potential for tracking total plaque volumes at standard macroscopic or intermediate resolutions, the current literature lacks optimized, high-resolution 3D baseline data and standardized segmentation workflows capable of resolving sub-cellular and micro-structural details. In this study, ex vivo CECT imaging is executed at an isotropic voxel size of 1.35 µm to provide a highly detailed spatial resolution for evaluating these murine plaques.

The general goal of this master's thesis is to test if high-resolution CECT imaging can successfully visualize and quantify plaque development in the AAV8-mPCSK9 mouse model. Using Hf-WD POM 1:2, the project aims to non-destructively map the different structures inside the intact aortic root. This study explores how effectively the components of the vascular wall can be separated based on their grayscale values, leveraging the calculated volumetric data to analyze the structural differences and lesion variations among the samples.

Part II

Methodology

Chapter 5

Materials and methods

5.1 Study design

The objective of this study is to enable detailed 3D visualization of the lesions and quantitative analysis of their development within the aortic root. The experimental model used involves the induction of atherosclerosis in mice via AAV8-mPCSK9 transduction and a high fat diet. All mice included in this study are female. Two groups were studied: a control group (n = 2; LS90 and LS93) and an early stage group (n = 3; LS58, LS59 and LS60), corresponding to an early stage of disease development, assessed 10 weeks after induction. After sample collection, the hearts were used as anatomical imaging units to facilitate sample manipulation during CECT scans. The analysis focused on the aorta, which is the primary region of interest (ROI) in the development of atherosclerotic plaques [34]. The entire experimental protocol includes a sample preparation phase (fixation, staining, and mounting), followed by high-resolution CECT imaging. The resulting data were reconstructed, preprocessed, and analyzed using segmentation to enable the quantification of vascular lesions.

5.2 Sample preparation

The preparation of samples was carried out in several successive steps to ensure adequate tissue fixation, good penetration of the contrast agent and optimal stability during CECT acquisitions. Initially, the samples were fixed for 48 hours in a 4% formalin solution to preserve the structural integrity of the tissues and limit the phenomena of post-mortem degradation. After fixation, all samples were transferred into a PBS solution and stored at 4 °C until the start of the experiments.

The staining step was then carried out using a 3.5% Hf-WD POM 1:2 solution, according to the protocol described by Pestiaux et al. [42]. The solution was prepared by dissolving 70 mg of the compound in 2 mL of PBS, followed by vortex agitation to ensure complete homogenization. The samples were then immersed in this solution and incubated for 10 days under agitation on a shaker plate, allowing a gradual and homogeneous diffusion of contrast within the tissues.

After staining, the samples were prepared for CECT imaging according to a procedure aimed at limiting movement and ensuring mounting stability. Each sample was first wrapped in parafilm to protect the tissue. An aluminum foil was then added to the sample to serve as a reference for the normalization of the gray values. The samples were placed in a sample holder filled with a gelose, prepared from 0.2 g of agarose dissolved in 10 mL of water, to ensure their mechanical support. The whole was then again wrapped in parafilm to secure the assembly. Finally, a cooling system was used during the acquisition, with a temperature maintained at -5 °C, in order to reduce sample movements and limit artefacts.

5.3 CECT image acquisition and reconstruction

The CECT acquisitions were carried out using a Phoenix NanoTom M® system (GE Measurement and Control Solutions, Wunstorf, Germany), controlled via the Phoenix datos|x acquisition software (Waygate Technologies, Baker Hughes, Houston, USA). All acquisition parameters were kept constant between samples to ensure direct comparability of data between different experimental groups. The samples were carefully positioned in the imaging system to ensure their stability and optimize acquisition quality. Particular attention was paid to reducing movements during the scan, notably thanks to the assembly of the samples described above and the use of a cooling system.

The images were acquired at high resolution, allowing a fine visualization of vascular structures and contrast agent deposition areas. Each scan was then reconstructed in order to generate 3D volumes that could be used for analysis. This step was carried out using the Phoenix datos|x reconstruction software (Waygate Technologies, Baker Hughes, Houston, USA), with identical parameters for all samples. The acquisition and reconstruction parameters used in this study are summarized in the Table 5.1.

Table 5.1: Summary of CECT acquisition and reconstruction parameters used for all samples.

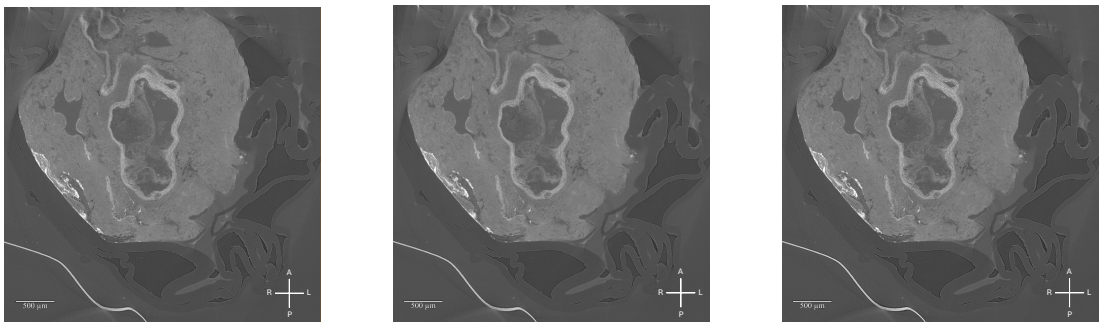
Parameter	**Value**
Scanner	Nanotom M (Waygate Technologies)
Acquisition software	Phoenix datos|x acquisition
Tube voltage	75 kV
Tube current	75 µA
Voxel size	1.35 µm
Exposure time	1250 ms
Number of projections	4200
Averaging	3
Skip	1
Scan duration	6 h
Focus-detector distance	600 mm
Focus-object distance	8.1 mm
Reconstruction software	Phoenix datos|x reconstruction
Scan optimizer	Yes
Beam hardening correction	7
Filters	Inline median, ROI-CT, Volume filter

5.4 Image preprocessing

A preprocessing pipeline was applied to the reconstructed image stacks to improve intensity consistency and enhance the structural visibility. A global intensity normalization was first performed to reduce inter-scan variability and allow the comparison between samples. This normalization was based on two reference materials present in the imaging field: an aluminium foil and parafilm. These materials were used to define a standardized intensity scale across datasets.

To reduce salt and pepper noise and local intensity fluctuations while preserving structural boundaries, a 3D median filter was applied using the Filter Sandbox module in Avizo software (Thermo Fisher Scientific, Waltham, Massachusetts, USA). The filter was applied in 3D with a 26-neighborhood connectivity and an iterative scheme (3 iterations). This configuration was chosen to ensure isotropic smoothing across the volumetric dataset while limiting excessive blurring of edges

(Figure 5.1b). To enhance local contrast and improve boundary definition after the median filter, an unsharp masking filter was applied. The filter was applied in 3D using a neighborhood size of 5 pixels, an edge contrast factor of 0.5, and a brightness threshold of 0. This step enhanced intensity transitions while preserving global intensity distribution (Figure 5.1c).



(a) Raw CECT cross-sectional image

(b) Image after application of a median filter

(c) Final filtered image after applying an unsharp mask filter

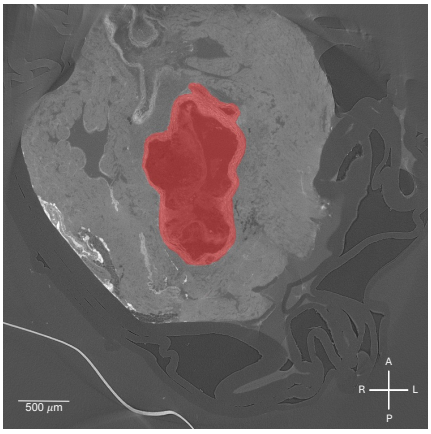
Figure 5.1: Pre-processing filtering steps illustrated using a representative cross-section (slice 777) of sample LS58. Scale bars: 500 µm. Anatomical orientation: A: anterior, P: posterior, L: left, R: right.

5.5 Image segmentation workflow

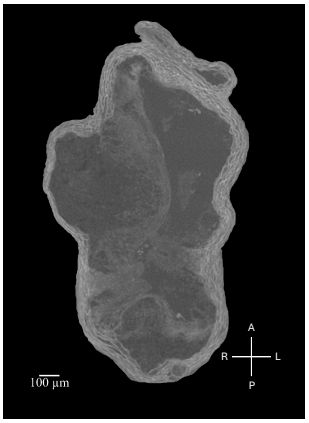
To isolate the aorta for the analysis, a multi-step segmentation workflow was developed using Avizo, combining manual region definition, gradient-based mathematical morphology, and intensity thresholding. The aortic ROI was first isolated from the reconstructed volumes (Figure 5.2a). A manual segmentation was performed using a brush-based tool in Avizo, combined with arithmetic operations, to separate the aortic structure from surrounding tissues and background (Figure 5.2b).

Several classical intensity-based segmentation methods, including k-means clustering, multilevel thresholding, and region-growing algorithms, were initially evaluated to partition the aortic ROI into distinct intensity-based regions. However, due to low contrast and overlapping intensity histograms, these methods did not provide robust or reproducible segmentations. Given these limitations, a marker-controlled watershed segmentation was implemented. First, an intensity gradient image was computed from the aortic ROI to enhance intensity transitions and emphasize

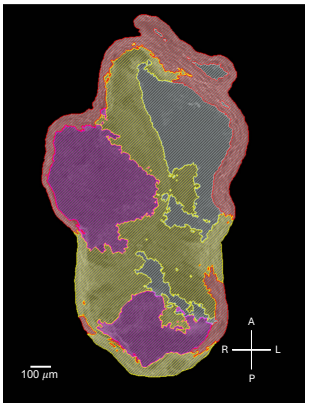
structural boundaries. To start the watershed algorithm, manual seed regions (markers) were defined on regularly spaced slices to ensure spatial coverage along the longitudinal axis. These seeding classes were distributed throughout the region of interest based on local grayscale variations and geometric landmarks. These annotations were used as initialization markers and were subsequently propagated to guide the segmentation in 3D. The watershed algorithm was executed using the computed gradient image as the topological surface and the manual seeds as initialization inputs. Among all initialization classes, only an internal void-like region was consistently and robustly segmented across all samples while other intensity-based regions showed limited spatial consistency (Figure 5.2c). To focus the analysis on the surrounding tissue of the aorta, the internal void region mask obtained from the watershed segmentation was removed from the aortic ROI, resulting in a residual volume corresponding to the vessel wall region (Figure 5.2d).



(a) Initial masking of the full aorta from the heart.



(b) Isolation of the full aorta from the heart.



(c) Multi-class segmentation result achieved via the watershed algorithm



(d) Final segmentation of the aorta.

Figure 5.2: Image segmentation workflow illustrated with a representative cross-section (slice 777) of the sample LS58. Scale bars: 100 µm (500 µm for (a)) Anatomical orientation: A: anterior, P: posterior, L: left, R: right.

Due to insufficient performance of automated clustering approaches within the vessel wall, a final segmentation was performed using manual intensity thresholding. Identical threshold values were consistently applied across all samples to ensure reproducibility and inter-sample comparability. The selected intensity intervals are summarized in Table 5.2. Thresholding started at an intensity value of 1 rather than 0, as voxels with a value of 0 in Avizo corresponded to regions outside the defined ROI. The threshold values were directly derived from a visual analysis of the intensity histograms, where boundaries were established by identifying recurring topological features such as peaks, valleys, and shoulders. Sample LS58 was selected as reference because it exhibited the clearest and most distinct separation between different intensity populations (Figure 5.3). Although small variations in intensity values were observed across the other early stage samples, the overall histogram morphology remained consistent. The additional histograms for LS59 and LS60 are provided in Appendix A. The same thresholds intervals were also applied to the control group to ensure unbiased comparison across all datasets (Figure 5.4). Control samples exhibited a more homogeneous intensity distribution characterized by two main peaks. When applying the same fixed thresholds, these broader peaks were subdivided into multiple intensity intervals. This subdivision is an inherent consequence of using a unified classification scheme across datasets with different structural complexity and was intentionally maintained to ensure consistency and avoid dataset-specific redefinition of intensity classes.

Table 5.2: Intensity ranges used for manual threshold-based segmentation.

Region	**Gray value**
Very low intensity region	1–75
Low intensity region	76–95
Medium-low intensity region	96–105
Medium-high intensity region	106–130
High intensity region	131-180
Very high intensity region	181–255

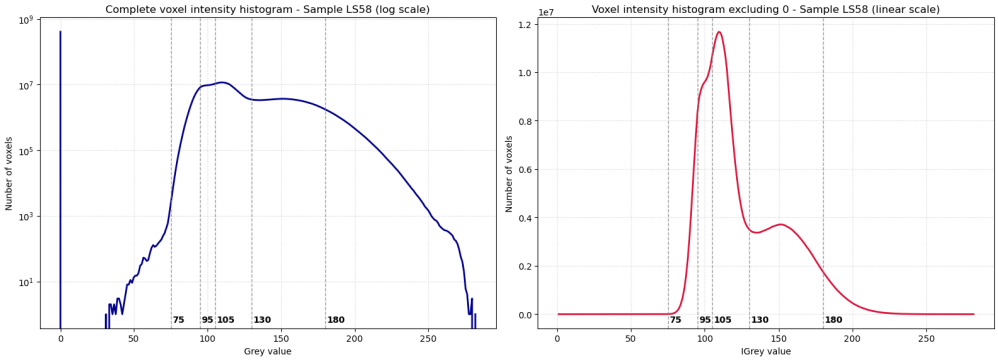


Figure 5.3: Grayscale intensity histograms of the CECT imaging of the early stage sample LS58 used to define thresholding values for multi-class segmentation. Left: Complete histogram plotted on a logarithmic scale. Right: Histogram plotted on a linear scale (excluding the peak at 0) to isolate the overlapping peaks. The vertical dashed lines indicate the selected multi-thresholding intensity values (75, 95, 105, 130, and 180).

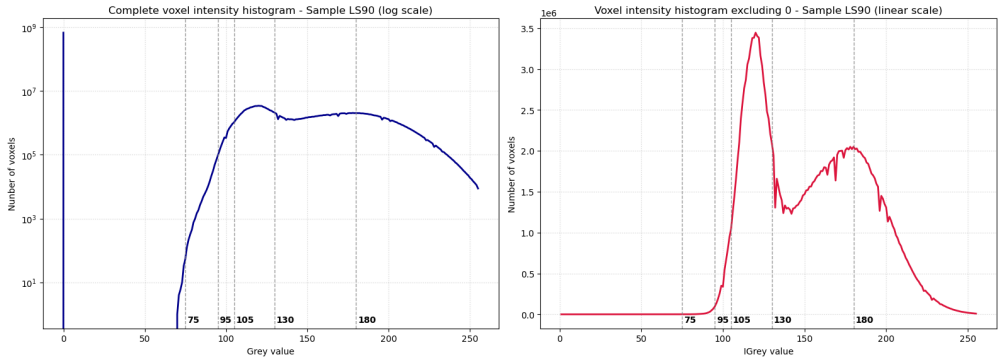


Figure 5.4: Grayscale intensity histograms of the CECT imaging of the control sample LS90 used to define thresholding values for multi-class segmentation. Left: Complete histogram plotted on a logarithmic scale. Right: Histogram plotted on a linear scale (excluding the peak at 0) to isolate the overlapping peaks. The vertical dashed lines indicate the selected multi-thresholding intensity values (75, 95, 105, 130, and 180).

Part III

Results and discussion

Chapter 6

Results

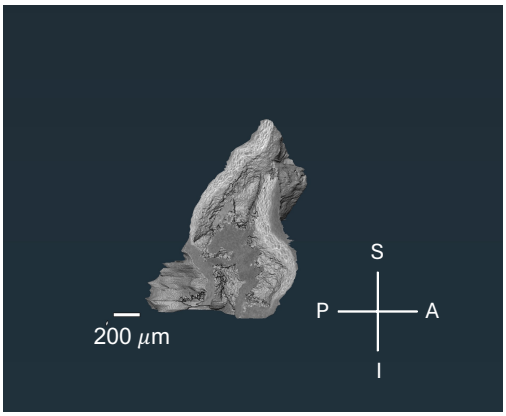
6.1 3D visualization of the aortic root

A qualitative assessment of the 3D architecture of the aortic root was performed to evaluate geometric and volumetric variations between the experimental groups. Representative 3D renderings and volumetric clipping sequences of a control sample and an early stage sample are illustrated in Figure 6.1 and Figure 6.2, with video sequences available via external repositories. The videos of the other samples are available in Appendix B.

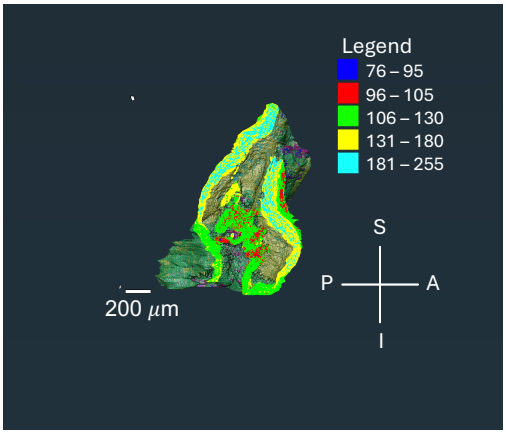
The 3D reconstructions reveal morphological differences between the two groups. First, the control aortic root (Figure 6.1) exhibits a more symmetric, smooth, and homogeneous geometry where the structural wall maintains a uniform thickness preserving the anatomy of the vessel. On the other hand, the volume rendering of the early stage sample (Figure 6.2) show geometric alterations characterized by severe asymmetric wall thickening. In this group, the tissue architecture appears irregular, with prominent bulging areas that cause a localized restriction of the vascular lumen.

To examine the internal spatial distribution of the different intensity regions, dynamic 3D clipping was applied sequentially along the coronal, sagittal, and transversal planes. This multi-planar internal analysis also highlights differences in the intramural voxel intensity distribution between the two conditions. In the control sample (Figure 6.1d), the cross-sectional views show that the vascular wall is predominantly composed of green and yellow voxels. There is also a small amount of light blue voxels confined inside the yellow voxels. This high-intensity distribution shows almost no signs of focal intramural low-attenuation areas. Conversely, the

internal clipping of the early stage sample exposes a more heterogeneous intramural composition (Figure 6.2d). The asymmetrically thickened regions are characterized by a massive, localized regions of low-intensity (dark blue and red) voxels. This distinct structural cluster is fully embedded within green and yellow voxels.



(a) 3D volume rendering

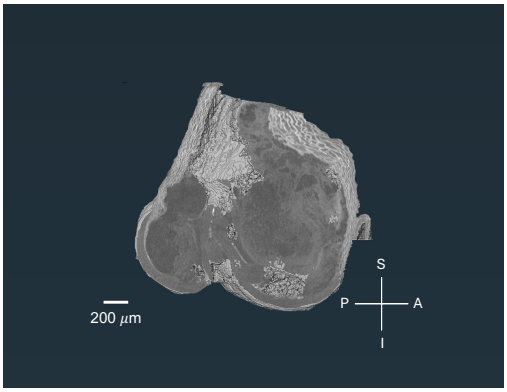


(b) 3D segmented volume rendering

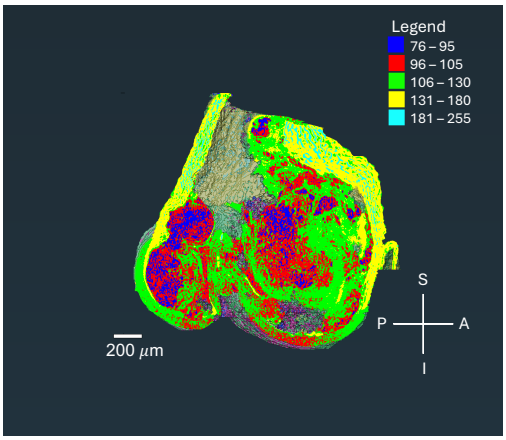
(c) `https://youtu.be/7cuylLzvI3c`

(d) `https://youtu.be/Sy3tUDpQ0Iw`

Figure 6.1: 3D visualization of a control sample (LS90). (a) Raw 3D CECT sagittal view. (b) Segmented 3D sagittal view showing density distribution. (c, d) QR codes to access the respective reconstructed videos. Scale bar: 200 µm. Anatomical orientation: S: Superior, I: Inferior, A: Anterior, P: Posterior.



(a) 3D volume rendering



(b) 3D segmented volume rendering

(c) `https://youtu.be/g8SCoQCk8sM`

(d) `https://youtu.be/BfjQfpDgwFQ`

Figure 6.2: 3D visualization of an early stage sample (LS58). (a) Raw 3D CECT sagittal view. (b) Segmented 3D sagittal view showing density distribution. (c, d) QR codes to access the respective reconstructed videos. Scale bar: 200 µm. Anatomical orientation: S: Superior, I: Inferior, A: Anterior, P: Posterior.

6.2 Intensity-based tissue classification

The absolute volumes measured for each grayvalue interval are summarized in Table 6.1, and their relative distribution is illustrated in Figure 6.3.

Table 6.1: Volumetric measurements (mm^3) of the defined gray value classes within the aortic wall for early stage (LS58, LS59, LS60) and control (LS90, LS93) samples.

	LS58	**LS59**	**LS60**	**LS90**	**LS93**
1-75	1,43e-05	1,14e-04	2,44e-05	2,68e-07	2,44e-04
76-95	0,098	0,13	0,10	7,86e-04	0,0023
96–105	0,27	0,21	0,29	0.02	0.034
106-130	0,39	0,21	0,42	0,16	0,19
131-180	0,35	0,18	0,23	0,20	0,24
181-255	0,054	0,00064	0,0015	0,13	0,23
Total	1,16	0,73	1,04	0,51	0,69

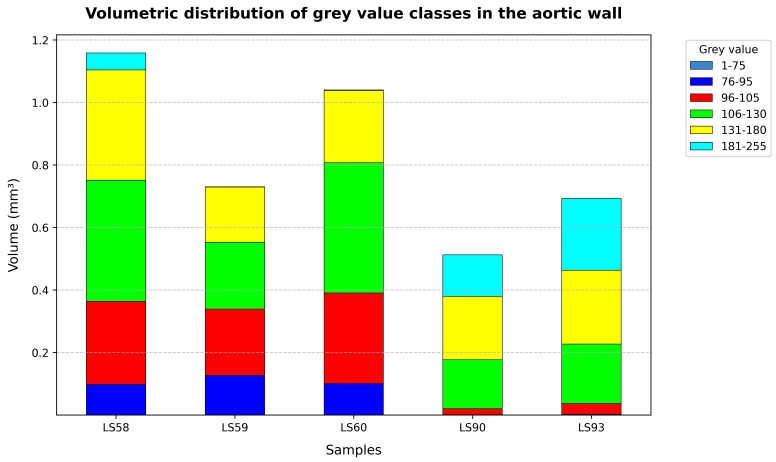


Figure 6.3: Cumulative bar chart highlighting the total volume and internal segmentation of the aortic wall for early stage (LS58, LS59, LS60) and control (LS90, LS93) samples.

The quantitative distribution profiles reveal marked differences in both total volume and internal composition between the early stage and control groups (Figure 6.3). First, the cumulative volume of the aortic root wall is consistently higher in the early stage samples. The total wall volume exceeds 1.0 mm^3 in LS58 and LS60, whereas all control specimens remain below 0.7 mm^3. Analysis of the intensity-class distribution further highlights substantial structural differences between both groups. The very low-intensity class (1–75) remains negligible across all datasets. The low-intensity class ranging from 76 to 95 is exclusively observed in the early stage samples, where it represents a significant fraction of the volume. In contrast,

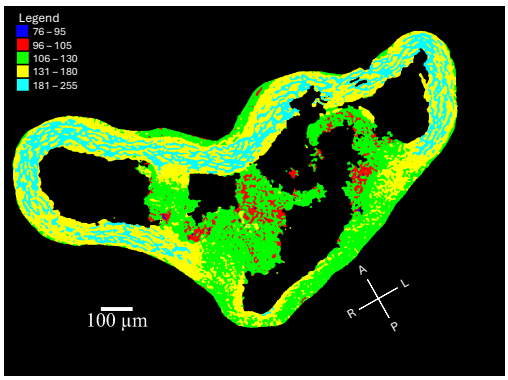
this class is rarely present and visually undetectable in the control samples.

The medium-intensity classes also show distinct distribution patterns between groups. The medium-low intensity region (96–105) occupies a considerable proportion of the wall volume in the early stage samples but is reduced to a thin residual layer in the controls. The medium-high intensity region (105–130) is present in both experimental groups. The high-intensity classes demonstrate a predominance of high-attenuation voxels within the control samples. The 131–180 gray value range represents the dominant volume fraction in control samples. Together with the very high-intensity class (181–255), these regions account for the majority of the volume. In the early stage group, the yellow class remains present, while the light blue class is limited to a thin layer and is nearly absent.

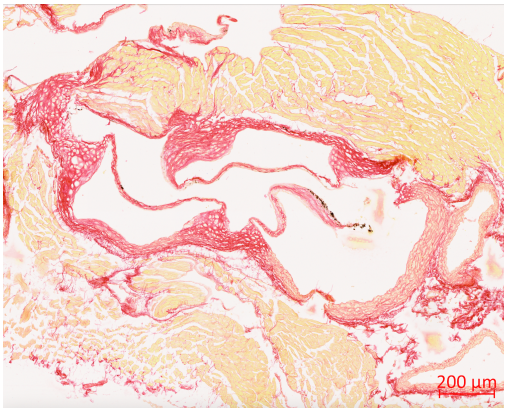
In summary, the application of a fixed thresholding baseline extracts a digital signature distinguishing the two biological conditions. The early stage group is characterized by a significant volumetric expansion driven by the emergence of lower attenuation profiles, while the control group exhibits a narrower distribution concentrated within the upper intensity ranges.

6.3 Histological correlation

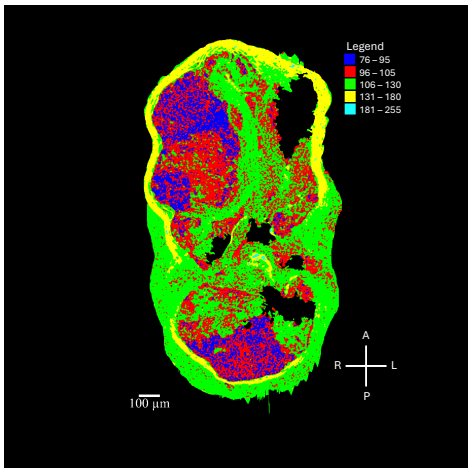
To establish a solid bridge between the computed 3D gray levels and the underlying pathological reality, a comparative qualitative analysis was conducted using classical 2D histology as a reference. Although the classical 2D histology sections were obtained from a distinct cohort of mice, these animals were subjected to a strictly identical atherosclerotic induction protocol AAV8-mPCSK9 transduction combined with 10 weeks of a high-fat diet), making them reliable biological replicas. Sections stained with Sirius Red were cross-referenced with representative CECT slices to corroborate the spatial distribution of the tissues and validate the specific threshold choices (Figure 6.4).



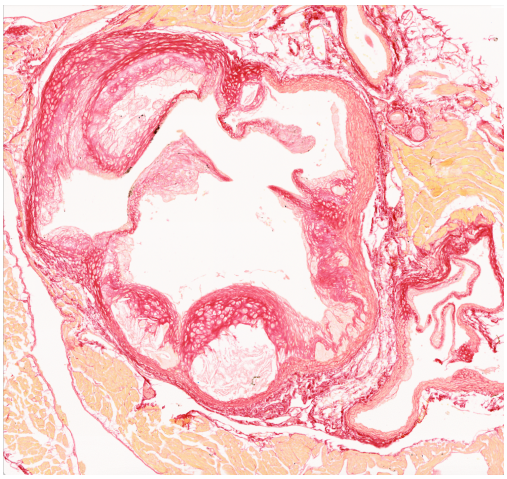
(a) Control CECT (LS90 - slice 1360)



(b) Control Sirius Red histology



(c) Early stage CECT (LS58, slice 1000)



(d) Early stage Sirius Red histology

Figure 6.4: Qualitative correlation between CECT cross-sections and reference 2D Sirius Red histological views. (a) Segmented CECT axial slice of a control sample (LS90, slice 1360) and (b) a control Sirius Red histological section. (c) Segmented CECT axial slice of an early stage sample (LS58, slice 1000) and (d) an early stage histological section. Scale bars: 100 µm (a, c), 200 µm (b, d). Orientation: A: anterior, P: posterior, L: left, R: right.

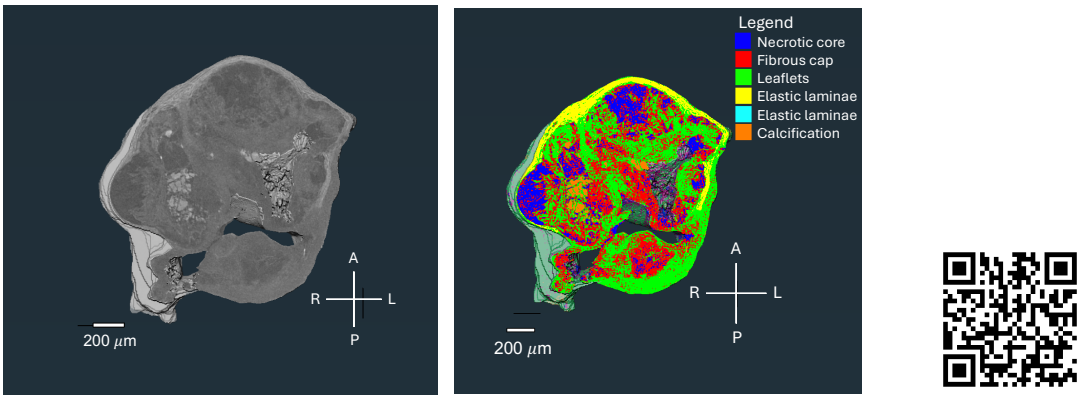
In the early stage group, the comparison between the Sirius Red histological sections (Figure 6.4d) and the CECT images (Figure 6.4c) reveals an organized and multilayered pathological structure. A spatial correspondence can be observed between the different gray-level intensity regions identified in the CECT datasets and the tissue composition visible in histology. In the CECT images, the lowest intensity range (1–75) is only present in very small areas and most likely corresponds

to image noise, reconstruction artifacts, or small remnants of the lumen previously removed and therefore do not seem to represent meaningful structural components of the lesion. In contrast, the low intensity range (dark blue voxels) forms a localized intramural region that spatially coincides with the large lipid-rich necrotic core visible on the Sirius Red sections. Around this low-intensity core, the medium-low range of the CECT images (red voxels) forms an intermediate layer that surrounds the dark blue voxels. On the histological sections, this region corresponds to the continuous fibrillar structure forming the developing fibrous cap. The spatial continuity of this layer suggests an active remodeling zone surrounding the necrotic core. The medium-high range (green voxels) is mainly distributed along the non-remodeled portions of the vessel wall. Anatomically, these regions correspond to preserved leaflets of the aorta and healthy valvular tissue. Finally, the highest intensity classes (yellow and light blue voxels), correspond to the most strongly attenuating structures within the vessel wall. These regions spatially align with the dense concentric elastic laminae of the tunica media observed in histology. In addition, several focal hyper-dense spots are visible within these high-intensity areas, suggesting localized regions with particularly elevated X-ray attenuation embedded within the surrounding elastic tissue.

In contrast to the heterogeneous profiles observed in the early stage group, the control samples exhibit a more regular and uniform vascular architecture (Figure 6.4a). The spatial distribution of the different gray-level classes follows a more stable, concentric geometric pattern, corresponding to the healthy tissue structures visible in the Sirius Red-stained histological sections (Figure 6.4b). Similarly to the early stage group, the lowest intensity range (1-75) remains extremely limited and no meaningful structural component appears to be associated with this class in the control samples. However, the intermediate intensity ranges between 76 and 130 (dark blue, red and green voxels) do not form focal intramural accumulations or localized wall thickening. Instead, these regions correspond to the normal anatomy of the healthy valvular leaflets. On the Sirius Red sections, these structures appear as thin and elongated valvular components. Their signal distribution remains continuous and homogeneous, without evidence of pathological remodeling. The highest intensity classes (yellow and light blue voxels) display a spatial distribution identical to that of the early stage group, constituting the majority of the healthy vessel wall volume. They form a continuous and concentric ring surrounding the lumen, which perfectly matches the preserved, compact organization of the tunica media's elastic laminae visible in histology.

6.4 Volumetric analysis of plaque components

Following the qualitative validation established through histological cross-referencing, a detailed quantitative morphometric analysis of the atherosclerotic lesions was performed exclusively for the early stage group (LS58, LS59, and LS60). As explained in section 6.3, the high-intensity ranges (131–180 and 181–255) obtained through automated thresholding do not represent a single tissue class, but rather capture a critical physico-chemical overlap between the stained elastin matrix and the hyper-dense pathologically calcified nodules. To resolve this limitation and prevent the severe underestimation of the total atherosclerotic burden, an architectural refinement was implemented. By coupling a 3D region-growing algorithm with a slice-by-slice manual editing procedure, the focal mineralized inclusions were geometrically uncoupled from the concentric tunica media. This tailored segmentation adjustment allows for the individual tracking and quantification of the calcified volume as an independent pathological phase, alongside the low-intensity necrotic core and the medium-low intensity fibrous cap. To illustrate this refined segmentation workflow and the spatial distribution of these newly individualized components, the early stage sample LS60 was selected due to its structurally advanced and macroscopically pronounced mineralized zones (Figure 6.5). The absolute volumes are summarized in Table 6.2 and the relative structural composition of the aortic roots of the early stage samples are represented in Figure 6.6.



(a) (b) (c)

Figure 6.5: CECT identification of calcified regions. (a) 2D structural view. (b) Segmented cross-section highlighting the calcifications (orange) embedded within the plaque tissue. (c) `https://youtu.be/kFWDeSqCTqs`. Scale bars: 200 µm. Orientation: A: anterior, P: posterior, L: left, R: right.

Table 6.2: Quantitative volumetric analysis (mm^3) of vascular wall and plaque components within the early stage group.

Component	**LS58**	**LS59**	**LS60**
Calcification	0,0068	0,001	0,011
Necrotic core	0,098	0.13	0.10
Fibrous cap	0.27	0.21	0.29
Valvular leaflet	0.39	0.21	0.42
Media's elastic laminae	0.40	0.18	0.22
Total volume	1.16	0.73	1.04

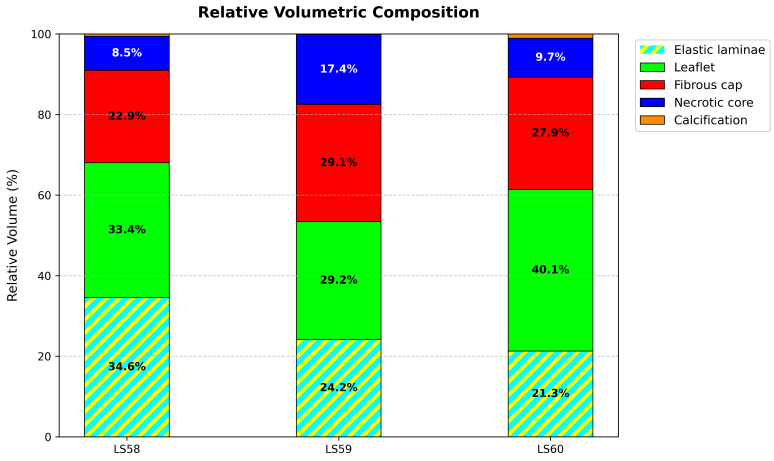


Figure 6.6: Relative volumetric composition of murine aortic root plaques. Stacked bar plot representing the percentage distribution of tissue components (Elastic laminae, Leaflet, Fibrous cap, Necrotic core, Calcification) for samples LS58, LS59, and LS60.

The quantitative distribution highlights a dominant structural pattern of healthy components across the samples, with the elastic media and valve leaflets collectively accounting for the majority of the total segmented volumes, ranging from 53.4% in LS59 to 68.0% in LS58. The analysis of the pathological fractions reveals volumetric trends as well as marked inter-individual phenotypic variations within this early stage cohort. For all three samples, the developing fibrous cap consistently remains the most significant pathological component, with relative volumes ranging from 22.9% (LS58) to 29.1% (LS59) the total aortic root volume.

A marked difference is observed regarding necrotic and mineralized components. Sample LS59 exhibits bigger necrotic core that accounts for 17.4% of the total volume, while its calcification remains statistically negligible at 0.1%. Conversely, sample LS60 reveals a more mineralized phenotype with the calcified nodules reaching an absolute volume of 1.1% of the total aortic root. This structural distribution in LS60 is visible in the dynamic 3D virtual sections (Figure 6.5c). The orange mineral clusters appear as dense intramural deposits that disrupt the leaflet (green voxels) and are closely associated with the necrotic core (dark blue voxels) and the fibrous cap (red voxels).

To further evaluate the vulnerability and severity of the remodeling within the early stage lesions, three standardized indices were computed from the refined volumetric data (Table 6.3).

Table 6.3: Plaque vulnerability and burden indices across the early stage group. Plaque burden: plaque volume/total vessel volume (%). Necrotic core volume fraction: Necrotic core volume/total plaque volume (%). Core-to-cap ratio: volume ratio between the necrotic core and the fibrous cap.

	LS58	**LS59**	**LS60**
Plaque burden (%)	32,1	46,6	38,5
Necrotic core volume fraction (%)	26,14	38,1	25
Core-to cap-ratio	0,36	0,62	0,34

The standardized indices confirm that despite having the lowest absolute total aortic volume, sample LS59 displays the highest proportion of plaque components. Its plaque burden reaches 46.6%, meaning nearly half of the entire vascular wall complex is occupied by atherosclerotic tissue. Furthermore, the necrotic core within LS59 occupies 38.1% of the total lesion volume, driving its core-to-cap ratio to a value of 0.62, nearly double the ratios calculated for LS58 (0.36) and LS60 (0.34). Conversely, while LS60 presented the most advanced calcified profile, its lower core-to-cap ratio reflects a larger proportion of fibrous cap relative to the necrotic core volume.

Chapter 7

Discussion

7.1 Physico-chemical basis of CECT and histological validation

The primary objective of this study was to evaluate the capacity of CECT to visualize and quantify the 3D architecture of atherosclerotic plaques. While microCT inherently excels at imaging highly attenuating mineralized structures, its application to soft tissues requires the introduction of CESAs to resolve different histological layers. To validate the biological identity of the gray-level classes obtained through manual thresholding, a direct qualitative correlation with classical 2D histology was made (See section 6.3).

The direct correlation between the gray levels observed in CECT and the colors visible in classical 2D histology originates from the complementary affinities of the contrast angents used in both imaging modalities. In histology, Sirius Red staining is commonly used to specifically visualize and quantify collagen fibers within the arterial wall and developing plaques [15]. Because collagen is a major component of fibrosis and ECM remodeling, Sirius Red provides a detailed overview of tissue organization and lesion architecture [45]. Beyond collagen itself, the staining also indirectly reveals SMC regions and lipid-rich zones through differences in structural appearance and contrast [15]. Similarly, the Hf-WD POM 1:2 diffuses into soft tissues, including muscle, connective tissue, ECM and blood-rich regions with a particularly strong affinity for elastin-rich structures [37]. From a physico-chemical standpoint, this overlapping retention is governed by the local macromolecular density of the ECM. Regions containing a dense, compact, and structurally preserved protein framework provide an abundance of chemical binding sites, causing both

staining agents to accumulate strongly. In histological sections, these dense matrix areas appear intensely red due to high Sirius Red binding to collagen fibers, while in CECT, the exact same regions exhibit elevated gray-level intensities due to the heavy concentration of high atomic number hafnium clusters within the uncompromised tissue architecture.

This density dependent retention is reflected when comparing the healthy tissue structures of the control group with the pathological remodeling in the early stage lesions. In control samples, the high and continuous binding of Hf-WD POM 1:2 highlights the dense, regular elastic laminae of the tunica media, which perfectly co-localizes with the red regions visible on Sirius Red sections. This close match confirms that in a healthy vascular state, the gray-level brackets between 131 and 255 serve as a reliable quantitative baseline for structural wall volume. Conversely, within the developing atherosclerotic plaques of the early stage group, the progressive disruption of the ECM drastically alters this staining pattern. The focal accumulations of lipids, cellular debris, and foam cells that constitute the necrotic core exhibit a highly disorganized and loose matrix structure. Consequently, these regions show a lower binding capacity for the Hf-WD POM 1:2, confining their signal to the lowest intensity range (76 to 95). Surrounding this core, the active recruitment of SMCs and the deposition of newly synthesized collagen fibers form the fibrous cap. This dense fibrotic remodeling promotes an intermediate accumulation of the contrast agent, generating a distinct signal in the medium-low gray-level range (96 to 105). By analyzing these configurations from a physico-chemical perspective, the intensity boundaries established in this study appear to reflect the local macromolecular integrity and pathological remodeling of the vascular wall.

7.2 Plaque characterization and volumetric interpretation of lesion vulnerability

Evaluating the physical expansion of a lesion serves as a primary dimensional parameter to quantify the overall atherosclerotic burden within the vessel wall [46]. In this study, the qualitative inclusion of the healthy control group provides a clear physiological reference. The CECT slices of control samples confirm the absence of any visible intraluminal disease, calcifications, or focal intima-media thickening. However, the quantified early stage lesions reveal structural differences that vary between the samples. Theoretically, the vascular wall can undergo positive or external remodeling, expanding its outer diameter to accommodate early plaque growth [46]. Nevertheless, the cross-sectional slices of all three early

stage samples already reveal a visible reduction and occlusion of the arterial lumen after only 10 weeks of high-fat diet induction. This generalized onset of luminal narrowing suggests that the volumetric expansion of the plaque is highly aggressive, progressively outpacing the compensatory remodeling capacity of the vessel and leading to measurable stenosis.

Within this pathologically altered cohort, the absolute physical expansion of the lesions remains variable between individual animals. For instance, sample LS59 exhibits the highest calculated plaque burden, with the plaques occupying nearly half of the entire vascular wall complex (46.6%). This elevated value, alongside the plaque volumes quantified in LS58 and LS60, highlights the morphological variations that can develop under identical experimental conditions. Together, these structural configurations demonstrate that while the aggressive nature of the plaque systematically leads to luminal narrowing, the precise quantitative burden fluctuates significantly from one animal to another.

Beyond the absolute size of the plaque, its internal composition plays a major role in determining whether the lesion remains mechanically stable or evolves toward a rupture phenotype [46]. Plaque vulnerability is largely governed by the balance between destabilizing components, mainly the lipid-rich necrotic core, and the protective structural elements of the lesion, particularly the fibrous cap. A large necrotic core combined with a thin fibrous cap is generally associated with a higher risk of rupture, whereas a more fibrotic and structurally organized plaque tends to reflect a more stable phenotype (see Section 1.1).

In this study, the standardized vulnerability indices reveal a similar mechanical balance between two of the main lesions identified in the cohort. Samples LS58 and LS60 exhibit very close core-to-cap ratios, reaching 0.36 and 0.34 respectively. From a structural perspective, this proximity suggests a comparable level of vulnerability, where the expansion of the necrotic core is counterbalanced by the overlying fibrous cap. However, despite these nearly equivalent ratios, a closer qualitative evaluation indicates that this equilibrium is achieved through distinct morphological pathways. LS58 displays a predominantly lipid-driven profile that resembles a classical early fibroatheroma. The lesion is characterized by the progressive accumulation of lipids and debris within the necrotic core, associated with a proportional fibrotic response. Without any evidence of mineral remodeling, the lesion retains the typical architecture of a vulnerable, lipid-rich plaque at an intermediate stage of progression. In contrast, LS60 presents a more mature and structurally consolidated phenotype. LS60 is characterized by the presence of focal micro-calcifications embedded within the extracellular matrix. These calcified regions introduce localized mechanical

heterogeneity that the global ratio cannot fully capture. Rather than representing a purely lipid-driven lesion, LS60 appears to be transitioning toward a fibro-calcific phenotype associated with a more complex and remodeled plaque architecture.

Within this framework, LS59 stands out as the most unstable lesion of the cohort. The sample exhibits a markedly elevated core-to-cap ratio of 0.62, driven by a large necrotic core occupying 38.1% of the total plaque volume. This pronounced imbalance evokes the structural characteristics of TCFA, where the protective fibrous cap progressively fails to compensate for the expanding necrotic burden beneath it.

Taken together, these observations show a broad heterogeneity generated within the mPCSK9 model. Rather than converging toward a single pathological endpoint, the lesions evolve along distinct structural trajectories, ranging from lipid-dominant vulnerable plaques to more mature fibro-calcific configurations. This diversity mirrors the variability observed in human ahterosclerosis formation and further supports the relevance of the model for studying both unstable and progressively stabilized plaque phenotypes within a relatively short experimental timeframe [46].

7.3 Analysis of tissue mineralization and calcification mapping

The isolation of a quantified mineralized volume in sample LS60 provides an opportunity to qualitatively evaluate the spatial distribution of early vascular calcification. To assess the translational relevance of this murine lesion, the CECT observations can be compared to the structural frameworks established for human fibrocalcific pathologies.

Despite the obvious differences in anatomical scale between human and murine tissues, the spatial topography of the mineral phase exhibits a notable biological consistency. In human valvular and vascular tissues, high-resolution 3D renderings demonstrate that early calcifications develop almost exclusively as intramural structures. These mineral deposits expand deep within the soft ECM rather than forming as extrinsic or superficial surface crusts [40]. The 3D segmentations and virtual cross-sectional slices of sample LS60 appear to corroborate this precise architectural behavior (Figure 6.5). The mineral clusters remain within the vessel wall and do not protrude into the arterial lumen. Instead, they are deeply embedded within the atherosclerotic plaque and anchor themselves against the dense tunica media. This shared topographical pattern suggests that the physico-chemical

constraints governing mineral deposition within a remodeling ECM follow preserved mechanical and biological pathways across species, supporting the translational value of the AAV8-mPCSK9 model.

Chapter 8

Conclusion and future perspectives

8.1 General conclusion

The primary objective of this master's thesis was to evaluate the capacity of CECT to visualize, segment, and quantify the 3D architecture of atherosclerotic lesions within the murine aortic root. By executing ex vivo CECT imaging at an advanced isotropic voxel size of 1.35 µm combined with the Hf-WD POM 1:2, this work provided a 3D digital baseline of the vascular wall. The implemented framework demonstrates that CECT imaging allows for a detailed assessment of the aortic root geometry. This approach successfully preserves the 3D continuity of the complex valvular and coronary structures.

Applying a unified digital preprocessing and manual thresholding pipeline to the cohort revealed clear structural differences between the biological conditions. The healthy control samples consistently exhibited a regular, thin, and concentric wall architecture restricted to the highest gray-level intensity ranges. In contrast, the early stage lesions displayed a substantial volumetric expansion driven by lower attenuation density profiles. Rather than converging toward a single uniform pathological endpoint, the three quantified early stage samples highlighted a heterogeneity developed under identical experimental conditions. This diversity closely mirrors the natural variability observed in human atherosclerosis formation, supporting the practical relevance of the AAV8-mPCSK9 model for preclinical imaging studies.

Within this heterogeneous cohort, the computed morphometric indices and qualitative 3D distributions allowed for a categorization of distinct lesion profiles. Sample LS58 displayed a predominantly lipid-driven profile that tends to reflect an early fibroatheroma configuration. It was characterized by a localized accumulation of low-attenuation lipidic components and necrotic debris, balanced by a standard fibrotic response. Conversely, sample LS59 stood out as a more aggressive phenotype. It exhibited a critical core-to-cap ratio of 0.60 and a high plaque burden, strongly evoking the morphology of a vulnerable thin-cap fibroatheroma. Finally, the internal architecture of sample LS60 presented a transitional signature shifting toward a consolidated fibro-calcific framework. This lesion was characterized by a distinct focal mineralization phase embedded within the soft remodeled wall.

8.2 Methodological and biological limitations

Despite a good visualization of the aortic root architecture, several biological and methodological limitations must be acknowledged. The primary limitation of this study lies in the 3D segmentation workflow, which heavily relies on manual intervention and introduces operator-dependent subjectivity. Tasks such as isolating the aorta from the rest of the heart using the brush tool or placing manual markers require user arbitration, limiting the overall reproducibility of the calculated volumes. Furthermore, establishing fixed intensity thresholds based on visual analysis of the intensity histograms represents a significant technical challenge. The histograms do not display perfectly distinct peaks and valleys, and their morphology varies from one dataset to another. This lack of consistency makes manual thresholding highly sensitive to slight variations between scans. The physical overlap between the heavily stained elastic matrix of the media and the early pathologically calcified clusters further illustrates this issue, demonstrating that a classification strategy based solely on grayscale values is insufficient to fully decouple overlapping tissue phases.

This lack of absolute biological specificity also impacts the experimental validation of the datasets. The histopathological sections used to guide the baseline definition were obtained from separate biological replicas rather than the scanned samples themselves. Consequently, an exact spatial alignment between the 2D histological slices and the 3D CECT volumes was not achievable. Without direct co-registration or complementary biochemical staining executed on the same scanned tissue, the biological identity assigned to each digital density class remains an indicative interpretation rather than a confirmation.

Finally, the characterization framework was restricted by a limited number of control samples (n=2). Although a third control specimen was originally included in the study design, technical constraints and system downtime during the acquisition phase prevented its completion. Scanning this remaining control sample would be necessary to confirm if the quantitative baseline and structural tendencies observed in the first two healthy specimens remain consistent.

8.3 Future perspectives

To address the methodological limitations identified in this work, several technical and experimental developments should be considered in future studies. First, to eliminate operator-dependent subjectivity and improve reproducibility, the integration of artificial intelligence and deep learning architectures could automate the 3D segmentation workflow. Training convolutional neural networks to isolate the aorta and extract the internal lumen would significantly reduce manual processing time and enhance dataset consistency. Furthermore, future image analysis strategies should expand beyond simple manual thresholding. Implementing texture analysis or multi-spectral microCT approaches could complement grayscale values, providing better discrimination between overlapping tissue components without relying solely on X-ray attenuation.

On an experimental level, the CECT framework established in this project opens the door for a comprehensive validation phase. Traditional 2D histology could be performed afterward on the same scanned aortic root samples to enable local structural correlations and provide a strict molecular validation of the density classes. Additionally, future work could implement advanced automated scripts to isolate and track every single calcium nodule individually, moving beyond global volumetric measurements. Following the multi-scale structural framework proposed by Pestiaux et al. [40], these mineralized clusters could be automatically quantified and classified based on their size, ranging from early micro-scale particles to larger consolidated deposits. Categorizing the individual distribution of these nodules would significantly refine the characterization of mineral kinetics and plaque stability over time in the AAV8-mPCSK9 model.

To fully exploit the potential of the morphometric profiling, the integration of advanced statistical models and additional geometric descriptors constitutes an other perspective. Future iterations of this pipeline should expand beyond global volumetric data by incorporating localized 2D and 3D measurements. Extracting regional features such as the maximum stenosis length, focal cross-sectional area

reductions, and spatial variations in cap thickness, will provide a more comprehensive, multi-dimensional characterization of lesion severity. Furthermore, applying a statistical analysis across the experimental groups will be essential to evaluate the robustness of these indices, enabling the identification of significant correlations between structural remodeling and plaque components within the cohorts.

Finally, expanding the biological study design represents a logical next step for this imaging framework. While the 10-week induction timeframe successfully revealed clear lesion heterogeneity and early calcification, incorporating an 18-week experimental timeframe will clarify the longitudinal progression of these phenotypes. This extension will determine whether the aggressive lipid-driven profiles evolve toward instability or transition into progressively stabilized fibro-calcific plaques.

Beyond its immediate preclinical relevance, the CECT framework established in this thesis carries translational implications. The ability to non-destructively resolve and quantify distinct plaque components, including the lipid-rich necrotic core, the protective fibrous cap, and early mineralized nodules, in 3D directly mirrors the structural features that clinicians seek to assess when stratifying cardiovascular risk in human patients. Current clinical imaging modalities, such as CT angiography or intravascular ultrasound, remain limited in their ability to simultaneously characterize soft tissue composition and calcification morphology at the microstructural level. While the high radiation doses and contrast agent requirements restrict this CECT pipeline to ex vivo preclinical research, the resulting 3D datasets highlight the value of high-resolution structural assessments. As imaging protocols and processing tools continue to evolve, achieving this level of 3D structural detail could gradually contribute to a better understanding of plaque morphology and tissue components in preclinical models

Appendix A

Additional segmentation results

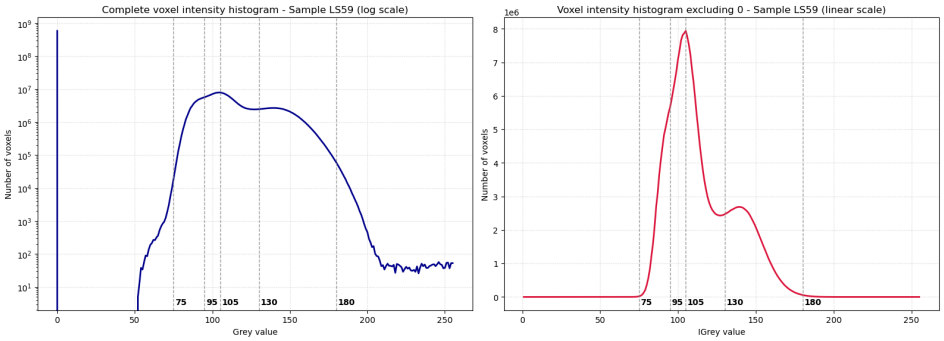


Figure A.1: Grayscale intensity histograms of the CECT imaging of the early stage sample LS59 used to define thresholding values for multi-class segmentation. (Left) Complete histogram plotted on a logarithmic scale. (Right) Histogram plotted on a linear scale (excluding the peak at 0) to isolate the overlapping peaks. The vertical dashed lines indicate the selected multi-thresholding intensity values (75, 95, 105, 130, and 180).

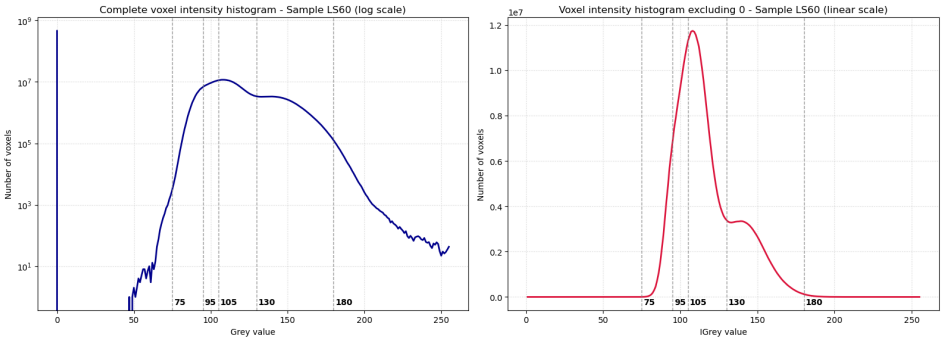


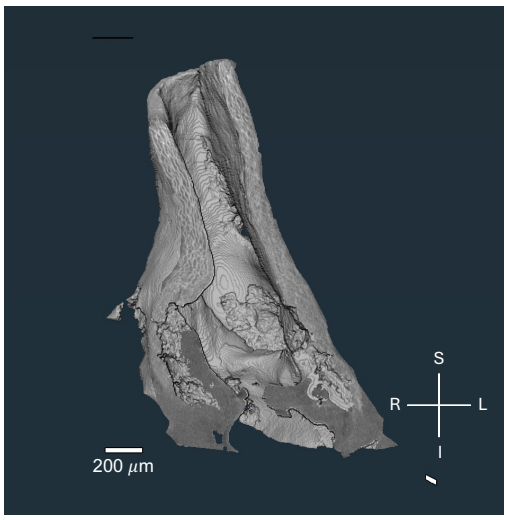
Figure A.2: Grayscale intensity histograms of the CECT imaging of the early stage sampe LS60 used to define thresholding values for multi-class segmentation. (Left) Complete histogram plotted on a logarithmic scale. (Right) Histogram plotted on a linear scale (excluding the peak at 0) to isolate the overlapping peaks. The vertical dashed lines indicate the selected multi-thresholding intensity values (75, 95, 105, 130, and 180).

Appendix B

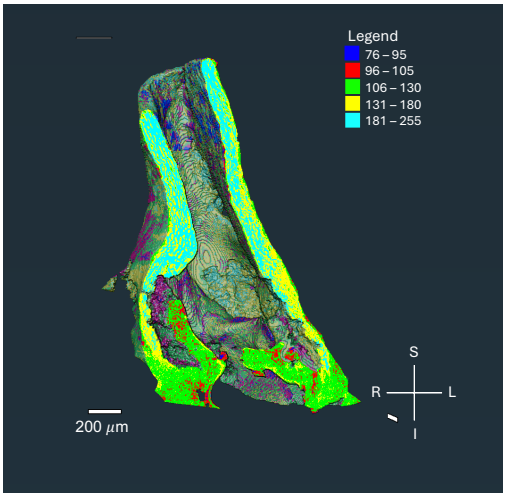
Additional 3D visualisation results



Figure B.1: QR code linking to the complete 3D visualization and video playlist of the analyzed aortic roots. `https://www.youtube.com/playlist?list=PLuRBcrA7AEgqrs15Br4lzea03sx2KtEGo`



(a) 3D volume rendering

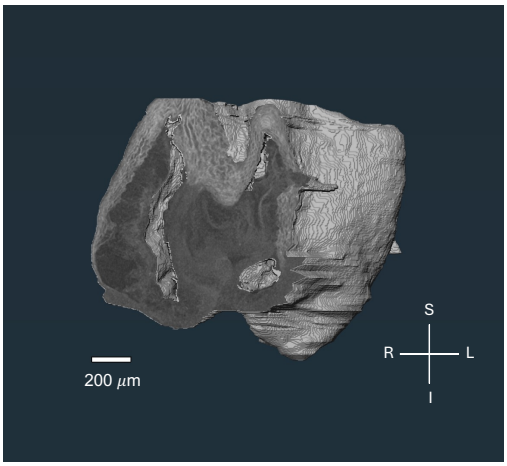


(b) 3D segmented volume rendering

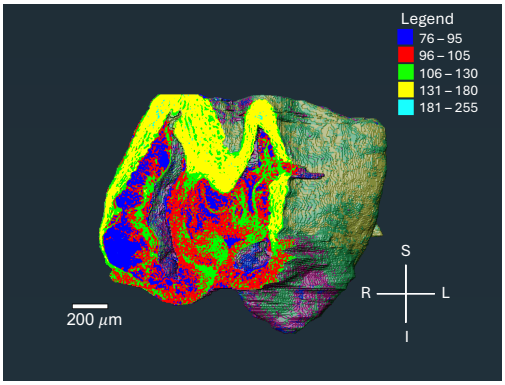
(c) `https://youtu.be/7cuylLzvI3c`

(d) `https://youtu.be/fegLqbs7UgM`

Figure B.2: 3D visualization of a control sample (LS93). (a) Raw 3D CECT coronal view. (b) Segmented 3D coronal view showing density distribution. (c, d) QR codes to access the respective reconstructed videos. Scale bar: 200 µm. Anatomical orientation: S: Superior, I: Inferior, R: Right, L: Left.



(a) 3D volume rendering

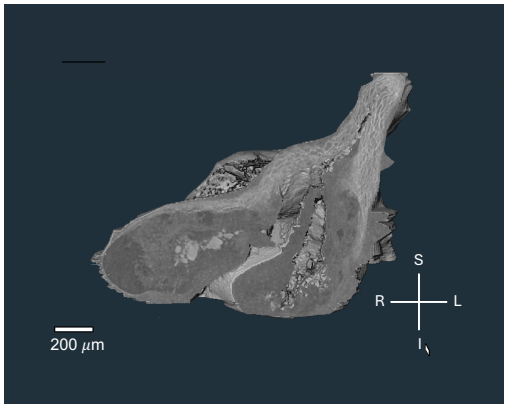


(b) 3D segmented volume rendering

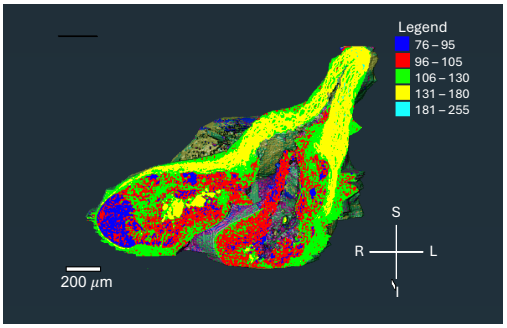
(c) `https://youtu.be/QISTBXB5U6I`

(d) `https://youtu.be/nAyhS3Pd4FE`

Figure B.3: 3D visualization of an early stage sample (LS59). (a) Raw 3D CECT coronal view. (b) Segmented 3D coronal view showing density distribution. (c, d) QR codes to access the respective reconstructed videos. Scale bar: 200 µm. Anatomical orientation: S: Superior, I: Inferior, R: Right, L: Left.



(a) 3D volume rendering



(b) 3D segmented volume rendering

(c) `https://youtu.be/UhOt7JG8zFU`

(d) `https://youtu.be/nUtucyXjJ24`

Figure B.4: 3D visualization of an early stage sample (LS60). (a) Raw 3D CECT coronal view. (b) Segmented 3D coronal view showing density distribution. (c, d) QR codes to access the respective reconstructed videos. Scale bar: 200 µm. Anatomical orientation: S: Superior, I: Inferior, R: Right, L: Left.

Bibliography

[1] B. Emini Veseli *et al.*, "Animal models of atherosclerosis," *SI:Atherosclerosis*, vol. 816, pp. 3–13, Dec. 5, 2017, ISSN: 0014-2999. DOI: 10.1016/j.ejphar.2017.05.010. [Online]. Available: https://www.sciencedirect.com/science/article/pii/S0014299917303205.

[2] A. Sarraju and S. E. Nissen, "Atherosclerotic plaque stabilization and regression: A review of clinical evidence," *Nature Reviews Cardiology*, vol. 21, no. 7, pp. 487–497, Jul. 1, 2024, ISSN: 1759-5010. DOI: 10.1038/s41569-023-00979-8. [Online]. Available: https://doi.org/10.1038/s41569-023-00979-8.

[3] I. Ilyas *et al.*, "Mouse models of atherosclerosis in translational research," *Trends in Pharmacological Sciences*, vol. 43, no. 11, pp. 920–939, Nov. 1, 2022, ISSN: 0165-6147. DOI: 10.1016/j.tips.2022.06.009. [Online]. Available: https://www.sciencedirect.com/science/article/pii/S0165614722001365.

[4] M. von Scheidt *et al.*, "Applications and limitations of mouse models for understanding human atherosclerosis," *Cell Metabolism*, vol. 25, no. 2, pp. 248–261, Feb. 7, 2017, ISSN: 1550-4131. DOI: 10.1016/j.cmet.2016.11.001. Accessed: Dec. 12, 2025. [Online]. Available: https://doi.org/10.1016/j.cmet.2016.11.001.

[5] J. I. v. d. Vaart, R. v. Eenige, P. C. N. Rensen, and S. Kooijman, "Atherosclerosis: An overview of mouse models and a detailed methodology to quantify lesions in the aortic root," *Vascular Biology*, vol. 6, no. 1, e230017, 2024, Place: Bristol, UK. DOI: 10.1530/VB-23-0017. [Online]. Available: https://vb.bioscientifica.com/view/journals/vb/6/1/VB-23-0017.xml.

[6] J. Aldana-Bitar, D. L. Bhatt, and M. J. Budoff, "Regression and stabilization of atherogenic plaques," *Trends in Cardiovascular Medicine*, vol. 34, no. 5, pp. 340–346, Jul. 1, 2024, ISSN: 1050-1738. DOI: 10.1016/j.tcm.2023.07.002. [Online]. Available: https://www.sciencedirect.com/science/article/pii/S1050173823000634.

[7] K. Kawai, R. Kawakami, A. V. Finn, and R. Virmani, "Differences in stable and unstable atherosclerotic plaque," *Arteriosclerosis, Thrombosis, and*

Vascular Biology, vol. 44, no. 7, pp. 1474–1484, Jul. 1, 2024. DOI: 10.1161/ATVBAHA.124.319396. Accessed: Dec. 16, 2025. [Online]. Available: https://doi.org/10.1161/ATVBAHA.124.319396.

[8] T. Kubo, "Optical coherence tomography in vulnerable plaque and acute coronary syndrome.," *Interventional Cardiology Clinics*, vol. 12, no. 2, pp. 203–214, 2023, ISSN: 2211-7458.

[9] R. A. van Dijk *et al.*, "Validating human and mouse tissues commonly used in atherosclerosis research with coronary and aortic reference tissue: Similarities but profound differences in disease initiation and plaque stability," *JVS-Vascular Science*, vol. 4, p. 100 118, Jan. 1, 2023, ISSN: 2666-3503. DOI: 10.1016/j.jvssci.2023.100118. [Online]. Available: https://www.sciencedirect.com/science/article/pii/S2666350323000226.

[10] A. Maier, A. J. P. Teunissen, S. A. Nauta, E. Lutgens, Z. A. Fayad, and M. M. T. van Leent, "Uncovering atherosclerotic cardiovascular disease by PET imaging," *Nature Reviews Cardiology*, vol. 21, no. 9, pp. 632–651, Sep. 1, 2024, ISSN: 1759-5010. DOI: 10.1038/s41569-024-01009-x. [Online]. Available: https://doi.org/10.1038/s41569-024-01009-x.

[11] R. Xing *et al.*, "Contrast-enhanced micro-CT imaging in murine carotid arteries: A new protocol for computing wall shear stress," *BioMedical Engineering OnLine*, vol. 15, no. 2, p. 156, Dec. 28, 2016, ISSN: 1475-925X. DOI: 10.1186/s12938-016-0270-2. [Online]. Available: https://doi.org/10.1186/s12938-016-0270-2.

[12] C. Goettsch *et al.*, "A single injection of gain-of-function mutant PCSK9 adeno-associated virus vector induces cardiovascular calcification in mice with no genetic modification," *Atherosclerosis*, vol. 251, pp. 109–118, 2016, ISSN: 0021-9150. DOI: https://doi.org/10.1016/j.atherosclerosis.2016.06.011. [Online]. Available: https://www.sciencedirect.com/science/article/pii/S0021915016302568.

[13] Z. Liu and S. Xu, "Assessing atherosclerosis in the aorta from AAV8-PCSK9-injected mice by oil red o staining," *JoVE*, no. 222, e68795, Aug. 8, 2025, ISSN: 1940-087X. DOI: 10.3791/68795. [Online]. Available: https://app.jove.com/68795.

[14] X. Zhang, S. Ha, W. Wei, S. Duan, Y. Shi, and Y. Yang, "Noninvasive imaging of aortic atherosclerosis by ultrasound biomicroscopy in a mouse model," *Journal of Ultrasound in Medicine*, vol. 34, no. 1, pp. 111–116, Jan. 1, 2015, ISSN: 0278-4297. DOI: 10.7863/ultra.34.1.111. Accessed: Mar. 9, 2026. [Online]. Available: https://doi.org/10.7863/ultra.34.1.111.

[15] L.-m. Gan *et al.*, "Non-invasive real-time imaging of atherosclerosis in mice using ultrasound biomicroscopy," *Atherosclerosis*, vol. 190, no. 2, pp. 313–320, 2007, ISSN: 0021-9150. DOI: https://doi.org/10.1016/j.atherosclerosis.

2006.03.035. [Online]. Available: https://www.sciencedirect.com/science/article/pii/S0021915006001821.

[16] L. Gan and Z. Wu, "Ultrasonography techniques for atherosclerosis assessment: A narrative review," *Iranian Red Crescent Medical Journal (IRCMJ)*, vol. 25, no. 7, 2023, ISSN: 2074-1804. DOI: 10.32592/ircmj.2023.25.7.2599. [Online]. Available: https://www.ircmj.com/article_189125.html.

[17] L. E. Mantella, K. Liblik, and A. M. Johri, "Vascular imaging of atherosclerosis: Strengths and weaknesses," *Atherosclerosis*, vol. 319, pp. 42–50, Feb. 1, 2021, ISSN: 0021-9150. DOI: 10.1016/j.atherosclerosis.2020.12.021. Accessed: Dec. 12, 2025. [Online]. Available: https://doi.org/10.1016/j.atherosclerosis.2020.12.021.

[18] A. Gallino *et al.*, ""in vivo" imaging of atherosclerosis," *ATHEROSCLEROSIS*, vol. 224, no. 1, pp. 25–36, Sep. 2012, ISSN: 0021-9150. DOI: 10.1016/j.atherosclerosis.2012.04.007.

[19] L. Ye, C.-C. Chang, Q. Li, Y. Tintut, and J. J. Hsu, "Advanced imaging techniques for atherosclerosis and cardiovascular calcification in animal models," *Journal of Cardiovascular Development and Disease*, vol. 11, no. 12, p. 410, 2024, ISSN: 2308-3425. DOI: 10.3390/jcdd11120410.

[20] D. B. Weinreb, J. G. S. Aguinaldo, J. E. Feig, E. A. Fisher, and Z. A. Fayad, "Non-invasive MRI of mouse models of atherosclerosis," *NMR in Biomedicine*, vol. 20, no. 3, pp. 256–264, May 1, 2007, ISSN: 0952-3480. DOI: 10.1002/nbm.1148. Accessed: Dec. 12, 2025. [Online]. Available: https://doi.org/10.1002/nbm.1148.

[21] R. C. Wüst, C. Calcagno, M. R. Daal, A. J. Nederveen, B. F. Coolen, and G. J. Strijkers, "Emerging magnetic resonance imaging techniques for atherosclerosis imaging," *Arteriosclerosis, Thrombosis, and Vascular Biology*, vol. 39, no. 5, pp. 841–849, May 1, 2019. DOI: 10.1161/ATVBAHA.118.311756. Accessed: Dec. 12, 2025. [Online]. Available: https://doi.org/10.1161/ATVBAHA.118.311756.

[22] E. Meester *et al.*, "Perspectives on small animal radionuclide imaging; considerations and advances in atherosclerosis," *FRONTIERS IN MEDICINE*, vol. 6, Mar. 11, 2019, ISSN: 2296-858X. DOI: 10.3389/fmed.2019.00039.

[23] A. Bassir, W. Y. Raynor, P. S. U. Park, T. J. Werner, A. Alavi, and M.-E. Revheim, "Molecular imaging in atherosclerosis," *Clinical and Translational Imaging*, vol. 10, no. 3, pp. 259–272, Jun. 1, 2022, ISSN: 2281-7565. DOI: 10.1007/s40336-022-00483-y. [Online]. Available: https://doi.org/10.1007/s40336-022-00483-y.

[24] B. Hammad, N. R. Evans, J. H. Rudd, and A. Tawakol, "Molecular imaging of atherosclerosis with integrated PET imaging," *Journal of Nuclear Cardiology*, vol. 24, no. 3, pp. 938–943, Jun. 1, 2017, ISSN: 1071-3581. DOI: 10.1007/

s12350-016-0766-y. [Online]. Available: https://www.sciencedirect.com/science/article/pii/S1071358123065789.

[25] A. M. F. Hag, R. S. Ripa, S. F. Pedersen, R. P. Bodholdt, and A. Kjaer, "Small animal positron emission tomography imaging and in vivo studies of atherosclerosis," *Clinical Physiology and Functional Imaging*, vol. 33, no. 3, pp. 173–185, May 1, 2013, ISSN: 1475-0961. DOI: 10.1111/cpf.12017. Accessed: Dec. 12, 2025. [Online]. Available: https://doi.org/10.1111/cpf.12017.

[26] X. Zhuang, Y. Feng, J. Li, F. Zhao, Y. Zhang, and Y. Chen, "A longitudinal 18f-fluorodeoxyglucose (18f-FDG) and 18f-sodium fluoride (18f-NaF) positron emission tomography/computed tomography (PET/CT) study in apolipoprotein e (ApoE) knockout rats fed with a western diet," *Cardiovascular Diagnosis and Therapy*, vol. 11, no. 1, 2021. [Online]. Available: https://cdt.amegroups.org/article/view/62033.

[27] B. Ferraro, P. Giustetto, O. Schengel, L. Weckbach, L. Maegdefessel, and O. Soehnlein, "Longitudinal in vivo monitoring of atheroprogression in hypercholesterolemic mice using photoacoustic imaging," *Thrombosis and Haemostasis*, vol. 0, Jan. 2023. DOI: 10.1055/a-2005-8784.

[28] Z. Xie *et al.*, "In vivo assessment of inflammation in carotid atherosclerosis by noninvasive photoacoustic imaging.," *Theranostics*, Mar. 26, 2020. DOI: doi:10.7150/thno.41211.

[29] C. Pestiaux, "Advanced x-ray-based 3d microstructural characterization of the heart and heart valves," Ph.D. dissertation, UCLouvain, Sep. 2023.

[30] R. L. Reddick, S. H. Zhang, and N. Maeda, "Atherosclerosis in mice lacking apo e. evaluation of lesional development and progression.," *Arteriosclerosis and Thrombosis: A Journal of Vascular Biology*, vol. 14, no. 1, pp. 141–147, Jan. 1, 1994. DOI: 10.1161/01.ATV.14.1.141. Accessed: Dec. 13, 2025. [Online]. Available: https://doi.org/10.1161/01.ATV.14.1.141.

[31] C. Jia *et al.*, "Notoginsenoside r1 attenuates atherosclerotic lesions in ApoE deficient mouse model," *PLOS ONE*, vol. 9, no. 6, pp. 1–9, Jun. 2014. DOI: 10.1371/journal.pone.0099849. [Online]. Available: https://doi.org/10.1371/journal.pone.0099849.

[32] H. Hartwig *et al.*, "Atherosclerotic plaque destabilization in mice: A comparative study," *PLOS ONE*, vol. 10, no. 10, e0141019, Oct. 22, 2015. DOI: 10.1371/journal.pone.0141019. [Online]. Available: https://doi.org/10.1371/journal.pone.0141019.

[33] M.-A. Shibata, E. Shibata, K. Maemura, Y. Kondo, and M. Harada-Shiba, "Pathological and molecular analyses of atherosclerotic lesions in ApoE-knockout mice," *Medical Molecular Morphology*, vol. 50, no. 3, pp. 130–144,

Sep. 1, 2017, ISSN: 1860-1499. DOI: 10.1007/s00795-017-0154-y. [Online]. Available: https://doi.org/10.1007/s00795-017-0154-y.

[34] S. Oppi, T. Lüscher, and S. Stein, "Mouse models for atherosclerosis research-which is my line?" *FRONTIERS IN CARDIOVASCULAR MEDICINE*, vol. 6, Apr. 12, 2019, ISSN: 2297-055X. DOI: 10.3389/fcvm.2019.00046.

[35] N. Coté *et al.*, "Inflammation is associated with the remodeling of calcific aortic valve disease," *Inflammation*, vol. 36, no. 3, pp. 573–581, Jun. 1, 2013, ISSN: 1573-2576. DOI: 10.1007/s10753-012-9579-6. [Online]. Available: https://doi.org/10.1007/s10753-012-9579-6.

[36] G. Kerckhofs, "Radiography and CT," UCLouvain, 2024.

[37] T. Balcaen, S. Vangrunderbeeck, W. De Borggraeve, and G. Kerckhofs, "Contrast-enhancing staining agents for ex vivo contrast-enhanced computed tomography: A review," *Tomography of Materials and Structures*, vol. 7, p. 100 052, Mar. 1, 2025, ISSN: 2949-673X. DOI: 10.1016/j.tmater.2025.100052. [Online]. Available: https://www.sciencedirect.com/science/article/pii/S2949673X25000051.

[38] L. Leyssens, C. Pestiaux, and G. Kerckhofs, "A review of ex vivo x-ray microfocus computed tomography-based characterization of the cardiovascular system," *International Journal of Molecular Sciences*, vol. 22, no. 6, p. 3263, 2021, ISSN: 1422-0067. DOI: 10.3390/ijms22063263.

[39] D. J. Lloyd *et al.*, "A volumetric method for quantifying atherosclerosis in mice by using MicroCT: Comparison to en face," *PLOS ONE*, vol. 6, no. 4, e18800, Apr. 18, 2011. DOI: 10.1371/journal.pone.0018800. [Online]. Available: https://doi.org/10.1371/journal.pone.0018800.

[40] C. Pestiaux *et al.*, "3d histopathology of stenotic aortic valve cusps using ex vivo microfocus computed tomography," *Frontiers in Cardiovascular Medicine*, vol. Volume 10 - 2023, 2023, ISSN: 2297-055X. DOI: 10.3389/fcvm.2023.1129990. [Online]. Available: https://www.frontiersin.org/journals/cardiovascular-medicine/articles/10.3389/fcvm.2023.1129990.

[41] D. Hoffmann *et al.*, "3d histological analysis of soft tissues by contrast-enhanced x-ray microfocus computed tomography: Screening and staining optimization of contrast-enhancing staining agents," *Microscopy and Microanalysis*, vol. 31, no. 2, ozaf013, Apr. 1, 2025, ISSN: 1431-9276. DOI: 10.1093/mam/ozaf013. Accessed: Dec. 17, 2025. [Online]. Available: https://doi.org/10.1093/mam/ozaf013.

[42] C. Pestiaux, A. Marino, L. Simal, S. Horman, R. Capoulade, and G. Kerckhofs, "X-ray-based 3d histology of murine hearts using contrast-enhanced microfocus computed tomography (CECT) and cryo-CECT," *Hearts*, vol. 5, no. 1, pp. 14–28, 2024, ISSN: 2673-3846. DOI: 10.3390/hearts5010002.

[43] L. Leyssens *et al.*, "MicroCT and contrast-enhanced microCT to study the in vivo degradation behavior and biocompatibility of candidate metallic intravascular stent materials," *Acta Biomaterialia*, vol. 191, pp. 53–65, 2025, ISSN: 1742-7061. DOI: https://doi.org/10.1016/j.actbio.2024.11.017. [Online]. Available: https://www.sciencedirect.com/science/article/pii/S174270612400672X.

[44] V. A. Stadelmann, G. Boyd, M. Guillot, J.-G. Bienvenu, C. Glaus, and A. Varela, "Automatic quantification of atherosclerosis in contrast-enhanced MicroCT scans of mouse aortas ex vivo," *International Journal of Biomedical Imaging*, vol. 2021, no. 1, p. 4 998 786, Jan. 1, 2021, ISSN: 1687-4188. DOI: 10.1155/2021/4998786. Accessed: Dec. 16, 2025. [Online]. Available: https://doi.org/10.1155/2021/4998786.

[45] A. Maes *et al.*, "Cryogenic contrast-enhanced microCT enables nondestructive 3d quantitative histopathology of soft biological tissues," *Nature Communications*, vol. 13, no. 1, p. 6207, Oct. 20, 2022, ISSN: 2041-1723. DOI: 10.1038/s41467-022-34048-4. [Online]. Available: https://doi.org/10.1038/s41467-022-34048-4.

[46] N. Vatsa, C. Faaborg-Andersen, T. Dong, M. J. Blaha, L. J. Shaw, and R. A. Quintana, "Coronary atherosclerotic plaque burden assessment by computed tomography and its clinical implications," *Circulation: Cardiovascular Imaging*, vol. 17, no. 8, e016443, Aug. 1, 2024. DOI: 10.1161/CIRCIMAGING.123.016443. Accessed: Feb. 25, 2026. [Online]. Available: https://doi.org/10.1161/CIRCIMAGING.123.016443.

UNIVERSITÉ CATHOLIQUE DE LOUVAIN
École polytechnique de Louvain
Rue Archimède, 1 bte L6.11.01, 1348 Louvain-la-Neuve, Belgique | **www.uclouvain.be/epl**